Organization of central circuits for wind-guided olfactory navigation

Andrew M.M. Matheson[1], Aaron J. Lanz[1], Al M. Licata[1], Timothy A. Currier[1,2,†], Mubarak H. Syed[3], and Katherine I. Nagel[1,4*]

[1]Neuroscience Institute, NYU Medical Center, 435 E 30th St. New York, NY 10016, USA

[2]Center for Neural Science, NYU, New York, NY, 4 Washington Place, New York, NY 10003

[3]Department of Biology, 219 Yale Blvd NE, University of New Mexico, Albuquerque, NM 87131

† Present address: Dept. of Neurobiology, Stanford University, 299 W. Campus Drive, Stanford CA 94305

*Corresponding author. Email: katherine.nagel@nyumc.org

Abstract:

To navigate towards a food source, animals must frequently combine odor cues, that tell them what sources are useful, with spatial cues such as wind direction that tell them where the odor can be found. Previous studies have identified wind-direction inputs that provide spatial information to the *Drosophila* navigation center, but olfactory inputs to this structure have not been functionally characterized. Here we use a high-throughput behavioral screen to identify a pathway linking olfactory centers to a part of the navigation center called the fan-shaped body (FB). We show that neurons throughout this pathway promote upwind movement, but encode odor independent of wind direction. We identify a type of FB local neuron that receives input from both wind-encoding and odor-encoding pathways, integrates these cues, and drives turning behavior. Based on connectome data, we develop a computational model that shows how the architecture of the FB enables odor input to flexibly gate behavioral responses to wind direction. Our work supports a model in which spatial and non-spatial information enter the FB through anatomically distinct pathways, and are integrated in FB local neurons to promote context-appropriate navigation behaviors.

Introduction:

Searching for a resource such as food requires a number of neural computations. Food sources are often identified by smell, and information about which odors signal useful and noxious food sources can be acquired both on slow evolutionary timescales, and within the lifetime of an animal (Auer et al. 2020, Kobler et al. 2020). Effective food search must therefore combine innate and learned information about the quality or potential value of different odors. In natural environments, food odors are often transported on the wind, forming turbulent plumes (Murlis et al. 1992, Cardé and Willis, 2008). Within these plumes, odor concentration is often a poor cue to source direction (Crimaldi and Kossef 2001, Webster and Weissburg 2001, Celani et al. 2014). Thus, many organisms have evolved a strategy of using odor information to gate upwind (or upstream) movement to locate the source of an attractive odor (David et al. 1983, Wolf and Wehner, 2000, Page et al. 2011, van Breugel et al. 2014, Alvarez-Salvado et al. 2018). Navigation towards potential food sources thus requires integration of directional information about the prevailing wind, generally derived from mechanosensation or vision, with information about the identity and quality of odors carried on that wind (Alvarez-Salvado et al. 2018, van Breugel et al. 2014). Where these two types of information are integrated is not known for any species.

In the insect brain, several conserved central neuropils have been implicated in navigation and food search, but their precise roles in these behaviors are not clear (Fig. 1A). The mushroom body (MB) is required to form learned associations between odors and rewards or punishments (deBelle and Heisenberg, 1994, Hige et al. 2015b). Different subsets of MB output neurons (MBONs) promote approach and avoidance (Aso et al. 2014, Owald et al. 2015) and can encode learned odor information (Hige et al. 2015a). A number of putative mechanosensory inputs to the MB have been identified (Bates et al. 2020) and wind-related signals have been observed in certain MB compartments (Mamiya et al. 2008). Manipulations of dopaminergic input to the mushroom body can regulate odor-evoked wind orientation behavior (Handler et al. 2019). However, it is not known whether the MB represents directional signals as well as odor value signals to support navigation.

A second central neuropil, the lateral horn (LH), is thought to be required for innate olfactory behavior. A small population of LH output neurons (LHONs) have been shown to drive approach behavior and to integrate input from MBONs of different valence (Dolan et al. 2019, Schlegel et al. 2021). The LH receives mechanosensory input in a discrete ventral region that is distant from the input to approach-promoting neurons (Dolan et al. 2019, Bates et al. 2020). A specific LH pathway has been implicated in one form of odor-guided navigation—avoidance of geosmin (Huoviala et al. 2020). However, like the MB, it is not known whether the LH encodes direction signals along with odor information.

In contrast, the fan-shaped body (FB), a part of the *Drosophila* navigation center called the central complex, has been recently shown to receive wind direction information (Currier et al. 2020). Columnar inputs to the fan-shaped body (FB), known as PFNs, represent wind direction as a set of orthogonal basis vectors, and receive input from the lateral accessory lobe (LAL) via LNa neurons (Currier et al. 2020). Wind direction signals are strongest in PFNs targeting ventral layers of the FB (PFNa, p, and m in the hemibrain connectome, Scheffer et al. 2020). PFNs targeting more dorsal layers (PFNd and v) have recently been shown to encode optic flow (Lyu et al. 2020) and self-motion during walking (Lu et al. 2020). PFNs of all types show little sensitivity to odor stimuli (Currier et al. 2020), suggesting that this pathway mostly encodes flow and self-motion information independent of odor.

A distinct set of FB inputs, known as FB tangential cells, are anatomically downstream of the MB (Li et al. 2020, Scaplen et al. 2020), however most of these have not been functionally characterized. To date, few olfactory inputs to the FB have been described (Homberg, 1985). Large lesions to the FB disrupt visual navigation (Strauss and Heisenberg 1993), and activation of subsets of FB neurons can produce oriented locomotor behaviors in cockroaches (Martin et al. 2015). Numerous studies have explored the role of the FB in path integration (Stone et al. 2017, Hulse et al. 2021), visual navigation (Sun et al. 2020), and landmark-guided long-distance dispersal (Dacke et al. 2019, Honkanen et al. 2019). However, few studies have investigated whether this region might play a role in olfactory navigation (Sun et al. 2021).

Here we used an optogenetic wind-navigation paradigm, together with calcium imaging, to ask how these three regions (MB, LH, and FB) work together to promote olfactory navigation behavior. We show that a subset of attraction-promoting MB and LH neurons can evoke upwind movement. However, calcium imaging indicates that these neurons encode odor independent of wind direction, suggesting that integration occurs elsewhere. We next performed a large behavioral screen of FB inputs, finding that several different groups of FB tangential inputs, but not columnar PFNs, can drive upwind movement. Imaging from these upwind-promoting FB tangential inputs revealed that many of them respond to attractive odor in a non-directional manner. Finally, we identify a specific type of FB local neuron that receives input from both wind-sensitive PFNs and from odor-sensitive FB tangential cells. We show that these neurons, called hΔC cells, integrate odor and wind direction cues and can elicit turning behavior. Taken together, our data support an emerging model of the FB in which spatial direction cues and non-spatial context cues enter this region through distinct anatomical pathways, and are integrated by local neurons to generate context-specific navigation behaviors. We develop a computational model based on connectome data that shows how this could work for odor-guided wind navigation.

Results

An optogenetic paradigm to investigate the circuit basis of wind navigation behavior

To investigate the neural circuit basis of wind-guided olfactory navigation, we developed an optogenetic activation paradigm. We modified a set of miniature wind tunnels (Fig. 1B, Alvarez-Salvado et al. 2018) to present temporally-controlled red light stimuli as walking flies navigated in a laminar wind flow. To validate this assay, we asked whether optogenetic activation of olfactory receptor neurons (ORNs) with Chrimson could produce behavioral phenotypes similar to those observed with an attractive odor, apple cider vinegar (ACV). We found that broad activation of olfactory receptor neurons using either the orco, or the orco and IR8a co-receptor promoters together (Larsson et al 2004, Silbering et al. 2011) resulted in robust navigation behaviors similar to those observed with ACV (Fig. 1C,D, Fig. S1A). In response to either odor or light, flies ran upwind, generating an increase in upwind velocity. Following odor or light offset, flies initiated a local search, characterized by increased curvature (Fig. 1C,D). Neither behavior was observed in the absence of the orco-GAL4 or orco/IR8a-GAL4 driver, or when we expressed Chrimson under an empty-GAL4 or empty split-GAL4 driver (Fig. 1E, Fig. S1B). Silencing both orco and IR8a-positive ORNs using tetanus toxin abolished both upwind and search responses to odor (Fig. 1F, G). Thus, optogenetic activation can substitute for odor in producing both upwind orientation and offset search, and ORNs are required for these behavioral responses to odor.

ACV activates a subset of both orco+ and IR8a+ glomeruli (Jung et al, 2015). Although the behavioral phenotypes evoked by ACV and by optogenetic activation of ORNs were similar, they exhibited some subtle differences. ACV produced a stronger upwind response than optogenetic activation of orco+ ORNs in the same flies (Fig. S1A). However, the offset search behavior evoked by optogenetic activation orco-GAL4, or of orco/IR8a-GAL4, was more robust than that evoked by ACV (Fig. 1C,D, Fig. S1A). Moreover, activation of orco/IR8a+ ORNs in the absence of wind produced offset search without upwind orientation (Fig. S1C). These results indicate that upwind orientation can be evoked independently of offset search, and suggest that these two behaviors are driven by distinct but overlapping populations of olfactory glomeruli. Our results also support the notion that navigational motor programs are encoded by population activity in ORNs (Badel et al. 2016, Bell and Wilson, 2016). Activation of single ORN types known to be activated by ACV (Jung et al, 2015), did not generate significant upwind orientation or offset search. In addition, silencing of orco+ or IR8a+ ORNs alone did not abolish upwind orientation, but did reduce offset search (Fig. 1G, Fig. S1E). These data indicate that groups of ORNs must be activated together to promote upwind orientation and that substantial silencing of most olfactory neurons is required to abolish upwind movement in response to ACV.

A subset of LHONs and MBONs drive wind navigation behavior and encode a non-directional odor signal

We next asked whether activation of central neurons in the LH and MB could similarly produce wind navigation phenotypes. We activated several groups of LHONs and MBONs that were previously shown to produce attraction or aversion in quadrant preference assays (Aso et al. 2014, Dolan et al. 2019). We found that several of these neuron groups drove robust upwind movement when activated (Fig, 2A,B, Fig. S2A). Neurons promoting upwind movement included the cholinergic LHON cluster AD1b2 (labeled by LH1396, LH1538, and LH1539 (Fig. 2A), and the cholinergic MBON lines MB052B (labeling MBONs 15-19), MB077B (labeling MBON12), and MB082C (labeling MBONs 13 and 14, Fig. 2B). AD1b2 drivers and MB052B also elicited significant increases in offset curvature when activated (Fig. 2A,B), while activating individual MBONs within MB052B (MBONs 15-19) did not drive significant upwind movement (Fig. S2B). Silencing single MBON or LHON lines that drove navigation phenotypes did not abolish upwind movement in response to odor (Fig. S2C) consistent with models suggesting that odor valence is encoded by population output at the level of the MB (Owald and Waddell, 2015), and with our findings at the periphery that very broad silencing is required to eliminate behavioral responses to ACV.

We also identified MBONs that produced other navigational phenotypes. For example, the glutamatergic (inhibitory) MBON line MB434B (labeling MBONs 5 and 6), which was previously shown to produce aversion (Aso et al. 2014), generated downwind movement in our paradigm (Fig. 2C). Moreover, two MBON lines produced straightening (reduced curvature) in our paradigm (Fig. 2D) but no change in movement relative to wind (Fig. 2D, Fig. S2A,B): the GABAergic line MB112C (labeling MBON 11), which evoked attraction in quadrant assays, and the glutamatergic line MB011B (labeling MBONs 1,3,4), which evoked aversion (Aso et al. 2014). Overall, these results indicate that LH/MB outputs can drive coordinated “suites” of locomotor behavior that promote attraction or aversion in different environments. Several LHONs and MBONs redundantly drive upwind movement, a key behavior for attraction in windy environments, while other MBONs drive straightening, which promotes attraction in odor gradients (Schulze et al. 2015) or in response to familiar visual stimuli (Ardin et al. 2016). Subsets of attractive and aversive MBONs drive upwind and downwind movement, indicating that the MB can promote opposing behaviors.

Are the LHONs and MBONs that drive upwind movement themselves sensitive to wind direction, or do they encode a non-directional odor signal that is integrated with wind direction information downstream? To answer this question, we performed calcium imaging experiments from each of the lines that generated upwind movement in our paradigm, and used a manifold (Suver et al. 2019, Figure S2D) to present the same calibrated odor stimulus from 5 different directions. Across all four upwind-promoting lines (MB052B, LH1396, MB077B, and MB082C), we observed robust responses to ACV, but no tuning for wind

direction (Fig. 2E, Fig. S2E, ANOVA: $F(4,35)=0.35$, $p=0.8408$, $F(4,40)=0.3$, $p=0.8794$, $F(4,25)=0.2$, $p=0.9989$, $F(4,35)=0.67$, $p=0.6166$). This lack of tuning contrasted sharply with previous recordings from wind-tuned LNa neurons, which provide input to wind-tuned PFNs, and were imaged using the same apparatus (Currier et al. 2020). These neurons did show significant tuning, using the same statistical test applied here (ANOVA: $F(4,25)=11.28$, $p=5.92431e-05$). To compare tuning for wind direction, we computed a tuning index equal to the difference between response to stimuli from 90˚ and -90˚. LNa, but not any of the MB/LH lines showed significantly tuned responses (Fig 2E). Responses to odor in our MB/LH lines differed in magnitude and kinetics across lines and flies, but were typically consistent across trials (Fig. S2E). Strong but transient responses were observed in MB052B, while smaller tonic responses were observed in LH1396, MB082C, and MB077B (Fig. 2E). Overall, these experiments indicate that the attractive odor ACV is represented in a non-directional manner across the population of upwind-promoting neurons in the MB and LH.

Previous studies found that the α'3 compartment of the MB is responsive to airflow (Mamiya et al. 2008), and that α'3 dopamine neurons receive putative mechanosensory input from the WED (Bates et al. 2020). To test specifically whether α'3 MBONs show wind direction tuning, we performed whole-cell recordings from these neurons using the split-GAL4 line MB027B, while presenting odor from one side. We patched both ipsilateral and contralateral α'3 MBONs and found no significant difference in their response to ACV (Fig. 2F). Thus, although neurons in the MB and LH respond robustly to odor and are capable of evoking wind-guided navigation behavior, they do not encode a directional signal related to wind. This suggests that they instead encode an odor identity or value signal that is integrated with directional information downstream to produce an orientation command.

Multiple tangential FB inputs promote upwind movement and respond to odor

The FB is anatomically downstream of the MB and LH (Li et al. 2020, Scaplen et al. 2020) and has previously been shown to encode signals related to an animal's orientation in space, including wind direction (Currier et al. 2020). We therefore asked whether inputs to the FB are likewise capable of driving movement relative to wind direction. We first confirmed that the FB is anatomically downstream of our neurons of interest by performing anterograde trans-synaptic tracing (Talay et al. 2017) on two of our lines that drove upwind movement (MB052B and LH1396) and observed signal in the dorsal layers of the FB in both cases (Fig. 3A).

To ask whether the FB might play a role in wind-guided navigation, we performed an activation screen of 40 lines labeling FB input neurons, including dorsal and ventral FB tangential inputs, and columnar PFNs. We performed this screen using genetically blind flies (see Materials and Methods) and in the presence of teashirt-Gal80 (Clyne and Miesenbock, 2008) to reduce potential Chrimson expression in the ventral-nerve cord (VNC) (see Methods). We found that 4 lines labeling FB tangential inputs, but no lines labeling PFNs, generated

significant movement upwind (Fig. 3B). Two dorsal FB input lines that were previously shown to promote sleep (23E10 and 84C10, Donlea et al. 2014) did not produce any wind-oriented movement in our assay, although we did observe a decrease in groundspeed in 23E10. FB tangential lines driving upwind phenotypes targeted both dorsal and ventral layers of the FB (Fig. 4A), in some cases both (65C03, 12D12). We attempted to refine these lines by making split-Gal4 drivers from combinations of these hemidrivers, but only one of these, labeling a set of ventral FB tangential inputs, also drove an upwind phenotype (Fig. 3C). Most such combinations labeled only a very small number of neurons.

In addition to the lines identified through our screen, we identified the neuron FB5AB using the connectome (Fig. 3D,E). This single pair of neurons stood out as the only FB input that receives at least one direct synaptic input from each of the MBON lines with wind navigation phenotypes (Fig. 3D). In addition, FB5AB receives the largest number of di-synaptic LH inputs from ACV-responsive glomeruli of any FB input neuron (Fig. 3E, see Methods). We identified a GAL4 line that labels FB5AB neurons (21D07). As 21D07 labels some neurons in the antennal lobe, a primary olfactory area, we used the cell class-lineage intersection (CLIN, Ren et al. 2016) technique to limit expression of Chrimson to neurons in the FB (see Methods). High intensity light activation of this driver, which weakly but specifically labels FB5AB, also drove upwind orientation (Fig. 4C).

Overall, upwind velocity responses to FB tangential input stimulation were more persistent than those evoked by optogenetic activation in the MB and LH, continuing to promote upwind displacement after light offset (Fig 3F, S4A). We characterized the neurotransmitter phenotypes of each of the hits from our screen and found that most were cholinergic, and thus excitatory (Fig, S4B). As in the MB and LH, silencing of individual FB input lines that drove upwind movement was not sufficient to block upwind movement in response to odor (Fig. S4C). Together these results support the hypothesis that patterns of population activity in FB tangential inputs can promote upwind movement.

We next sought to characterize the sensory responses of upwind-promoting FB tangential inputs. We performed calcium imaging from all lines that drove upwind phenotypes, and imaged neural activity in the FB in response to wind and odor presented from different directions (Fig. 4A,B). We observed responses to ACV in all but one line (45D04). No FB tangential line showed significant directional tuning (ANOVA: 21D07: $F(4,40)=2.14$, $p=0.0938$, 65C03: $F(4,30)=0.68$, $p=0.6096$, 12D12: $F(4,25)=0.13$, $p=0.971$, vFB split: $F(4,25)=0.64$, $p=0.6358$) nor a significant difference between responses to stimuli from 90˚ and -90˚ (Fig 4D). The largest responses were observed in FB5AB (21D07), although these (but not other FB tangential line responses) decayed over trials (Fig 4E). In the line 65C03, we observed odor responses only from the dorsal layers of the FB, while in the line 12D12, we observed odor responses only from the ventral layers of the FB. Together these data identify a population of

olfactory FB tangential inputs, targeting multiple layers of the FB, that respond to attractive odor and promote upwind movement.

hΔC neurons integrate odor and wind direction signals and drive re-orientation

Our functional imaging data suggest that, like the upwind-promoting neurons in the MB and LH, FB tangential inputs are not strongly directionally tuned for wind. This contrasts with our previous survey of PFN columnar inputs to the FB (Currier et al. 2020), which showed strong directional tuning for wind in these cells— particularly those innervating ventral FB layers— but little modulation by odor. Together these data suggest that columnar and tangential inputs to the FB encode spatial (orientation-tuned) and non-spatial information respectively. We therefore hypothesized that FB local neurons, which receive input from both columnar and tangential inputs, might integrate these two types of information.

To identify FB local neurons that might integrate odor and wind direction signals, we used the hemibrain connectome (Scheffer et al. 2020) to search for neurons that receive input both from FB5AB and from the most wind-sensitive PFNs in our previous survey (PFNa, p, and m). This analysis revealed a population of 20 hΔC neurons that tile the vertical columnar structure of the FB (Fig. 5A, Hulse et al. 2021). Each hΔC neuron receives input from wind-sensitive PFNs at its ventral dendrites, and from FB5AB at its dorsal axons, where olfactory input might gate synaptic output (Fig. 5B,C).

To ask whether hΔC neurons integrate wind and odor signals, we identified a GAL4 line—VT062617— that labels hΔC neurons, and performed calcium imaging from the FB while presenting odor and wind from different directions. We observed calcium responses in the dorsal FB, where hΔC neurons form output tufts (Fig. 5D), thus we expect that these responses arise largely from output processes. In several examples, we observed odor responses that were strongest for a particular direction of wind (Fig. 5E). Similar to wind-sensitive PFNs, hΔC responses were strongest to +45 and -45° (Fig. 5F), although the relationship between wind direction and peak response was not consistent across flies (Fig. 5E). hΔC neurons responded more strongly to odor than to wind onset (Fig. 5G, Fig. S3B) and odor responses were typically localized to a few nearby columns (Fig. 5H). We found hΔC neurons to be cholinergic (Fig. S5B) and thus excitatory. These results are consistent with the idea that hΔC neurons receive and integrate both odor information and wind-direction information. In particular, they suggest that wind-direction tuned activity in hΔC neurons is gated on by odor information.

To determine whether hΔC neurons contribute to navigation, we generated two split-GAL4 lines that selectively label hΔC neurons. Activation of these lines caused flies to turn, resulting in an increase in curvature (Fig. 5I, Fig. S5C). No such increase in curvature was observed with empty-GAL4 or empty split-GAL4 drivers (Fig. 3C). We also observed a strong

turning phenotype when activating VT062617-GAL4 (Fig. S5C). Thus, hΔC neurons integrate wind direction and odor inputs and can drive re-orientation behavior.

The architecture of the FB suggests a model for olfactory gating of wind orientation

Our behavioral activation and functional imaging data, together with work from previous studies, support different roles for different anatomical input pathways to the FB. Columnar inputs to the FB, known as PFNs, carry directional cues such as wind direction (Currier et al. 2020), optic flow (Lyu et al. 2020), and self-motion (Lu et al. 2020), and while we show here that tangential inputs to FB carry odor information and can promote upwind orientation. How might FB tangential inputs allow flies to flexibly alter their orientation to wind?

To address this question, we developed a computational model of wind orientation circuitry, based on the known connectivity and response properties of FB neurons. The FB receives wind direction input through a subset of PFNs (Currier et al. 2020) and has been proposed to control steering motor output through PFL3 output neurons (Hulse et al. 2021, Rayshubskiy et al. 2020). We therefore hypothesized that competing pathways between these two groups of neurons might promote down- and up-wind orientation respectively, with odor input through FB5AB, and other FB tangential neurons, altering the balance of activity between these pathways. Wind-sensitive PFNs make both direct connections onto PFL3 neurons (Fig. 6A) and indirect connections onto PFL3 neurons via hΔC and FC neurons (Fig. 6B, Scheffer et al. 2020, Hulse et al. 2021). Thus, the connectivity of the FB supports the notion of competing pathways from wind direction input to pre-motor output, with the indirect pathway gated ON by odor input.

We next examined the relationship between wind direction and motor output in our behavioral data (Alvarez-Salvado et al. 2018). We plotted the average angular velocity as a function of wind orientation both at baseline (Fig. 6C) and in the presence of odor (Fig. 6D). In the wind-only condition (Fig. 6C), wind from the left (negative wind direction) promotes right turns (positive turn angle), leading to stable downwind orientation. In contrast, in the wind + odor condition (Fig. 6D), wind from the left promotes turns to the left, and vice-versa, leading to stable upwind orientation. Thus, up- and down-wind orientation reflect distinct mappings from wind input to steering motor output.

We then developed a model of how the direct and indirect pathways in the FB might differentially transform wind direction input into motor output. Based on anatomical and physiological data, we hypothesize that wind-sensitive PFNs in each hemisphere exhibit a bump of activity, located 45° contralateral to the fly's heading (Fig. 6e). Wind direction modulates the magnitude of these two bumps so that each bump is maximal when wind arrives from 45° ipsilateral to the fly, and maximally inhibited at 135° contralateral (Fig. 6F). This model is consistent with the known physiological responses of wind-sensitive PFNs (Currier et al. 2020),

and with the known connectivity between PFNs and compass neurons that encode the fly's heading (Hulse et al. 2021). It is also analogous to the representation of optic flow that has recently been described in other populations of PFNs (PFNd and v, Lyu et al. 2020). Because PFNs in each hemisphere converge in the FB (Hulse et al. 2021), these bumps will sum, producing a single peak of calcium activity in their downstream targets (pink curve in Fig. 6G). hΔC neurons receive PFN input at their dendrites, and make outputs half-way across the FB. Thus, the representation of wind direction in hΔC neurons will be shifted by 180° (red curve in Fig. 6G) compared to the representation in PFNs. The direct and indirect pathways therefore produce two competing wind representations in the FB that differ by 180°, much like behavioral orientation down- and upwind.

In our model, PFL3 neurons then translate these wind representations into steering commands (Stone et al. 2017, Rayshubskiy et al. 2020). As has been noted previously, these neurons are well-poised to ask whether a left or right turn would best bring the animal in line with its goal orientation (Stone et al. 2017, Hulse et al. 2021). This is because PFL3 neurons in each hemisphere each inherit a bump of calcium activity that is shifted by 90° to the left or right of the fly's heading (Hulse et al. 2021, Fig. 6H). By comparing the wind direction bump in either PFNs or hΔC neurons with these two PFL3 bumps, the fly can compute which direction of turning will bring it in line with its goal down- or up-wind. Mathematically, we do this by summing the bump of activity in PFNs (or hΔC neurons) with the two PFL3 bumps, and computing the ratio of activity in right and left PFL3 neurons. PFL3 neurons project contralaterally, and we assume they are inhibitory, so that greater activity in right PFL3 neurons produces a right turn.

We illustrate this process in Fig. 6 I-L. In the direct pathway (Fig. 6I), wind on the left produces a PFN bump that overlaps more closely with the right PFL3 bump, producing a right turn. When simulated for all possible wind directions, this model generates a downwind mapping between wind direction and motor output, similar in shape to the one measured experimentally (Fig. 6K, Fig. S4). In the indirect pathway (Fig. 6J), wind on the left produces a wind bump in hΔC that overlaps more closely with the left PFL3 sinusoid, producing a left turn. Across wind directions, this circuit generates an upwind mapping from wind direction to motor output (Fig. 6L, Fig. S6).

The computations used by this circuit to generate downwind or upwind orientations can be analogously described by representing left/right PFN bumps as vectors and then performing vector addition (PFN = PFN_{left} to PFN_{right}), vector rotation (hΔC = PFN + 180°), and vector projection (PFN/ hΔC → PFL3 vectors) (Fig. 6G ,I, J). A similar set of computations suggests that hΔC might also alter forward walking speed as a function of wind direction, mediated by PFL2 output neurons (Fig. S7). Overall, the circuit logic outlined here allows a non-directional value signal (carried by FB tangential inputs) to alter the relationship between directional input

(carried by wind-sensitive PFNs) and motor output (carried by PFL3 and PFL2), resulting in a change to the animal's target heading. Because FB tangential inputs such as FB5AB are downstream of both MB and LH neurons that promote wind orientation, they are poised to integrate innate and learned value signals to shape navigational trajectory selection (Fig. 7). However, the same logic could be applied for other non-directional FB tangential inputs to generate orientation with respect to optic flow or self-motion cues carried by other PFNs (Lu et al 2020, Lyu et al 2020). Our computational model thus illustrates how an integrated value signal carried by FB tangential inputs could be used to dynamically modulate navigation behavior (orientation and forward velocity) with respect to a variety of directional cues.

Discussion:

Spatial and non-spatial pathways for wind-guided olfactory navigation

Wind-guided olfactory navigation is an ancient and conserved behavior used by many organisms to locate odor sources in turbulent environments. Despite large differences in the types of odors they seek, and in the physics of odor dispersal, very similar behaviors have been observed in pheromone-tracking moths (Kennedy et al, 1974), food-seeking crustaceans (Page et al. 2011), and ants seeking both food and their nest (Buehlmann et al. 2012). Thus, this behavior is absolutely required in many animals for survival and reproduction, and likely mediated by conserved neural circuits.

In a previous study, we identified inputs to the FB that encode wind direction (Currier et al. 2020). Neurons throughout this pathway, including both LNa neurons and PFNs, show activity that is strongly modulated by wind direction, but little modulated by odor. Other LN and PFN neurons have been shown to strongly encode optic flow direction (Stone et al, 2017, Lyu et al. 2020), another cue that signals self-motion and wind direction— particularly in flight. Taken together, current data thus suggest that the columnar pathway to the FB encodes information about self-movement and environmental flow useful for recognizing where the fly is relative to its environment.

In contrast, the present study identifies an olfactory pathway to the FB that encodes odor information independent of the wind direction from which it is delivered. We found that neurons in both the MB (a center for associative learning) and the LH (a center for innate olfactory and multi-modal processing) are capable of driving upwind movement. However, none of these upwind-promoting neurons exhibited wind-direction tuned responses. Thus, the outputs of these regions likely represent odor identity or odor value signals, as has been suggested by several recent models (Ardin et al., 2016, Cognini et al., 2018). We further characterized a large population of olfactory tangential inputs to the FB that likewise promote upwind movement and encode odor independent of wind direction. At least one of these neurons is anatomically downstream of upwind-promoting MB and LH neurons. These data

are consistent with previous studies showing that other FB tangential inputs encode non-spatial variables such as sleep state (Donlea et al. 2014) and food choice (Sareen et al. 2021). Together, these data suggest that the pathway running from the MB/LH to the FB encodes non-spatial information.

The segregation of spatial and non-spatial FB inputs that we observe here shows some similarities to the organization of visual circuits in primates and of navigation circuits in rodents. In primate vision, processing of object identity and object location are famously thought to occur in distinct pathways (Mishkin et al. 1983). In the hippocampus, inputs from the medial entorhinal cortex have been shown to encode spatial cues, while anatomically distinct inputs from the lateral entorhinal cortex can encode non-spatial context cues, including odors (Hargeaves et al. 2005, Leitner et al. 2016). Thus, a segregation of spatial and non-spatial processing may be a general feature of central neural representations in both vertebrate and invertebrate brains.

What might be the advantages of this type of organization? One hypothesis is that it allows learning about non-spatial cues to be generalized to different spatial contexts. For example, during food-guided search, innate information about which odors signal palatable food must be integrated with learned odor associations (Hige et al. 2015b, Kobler et al. 2020, Schlegel et al. 2021), as well as with internal state variables such as hunger (Sayin et al. 2019, Sareen et al. 2021). However, the fly may wish to generalize information learned while walking to search in flight. In walking flies, wind direction can be computed directly from mechanosensors in the antennae (Bell and Kramer, 1979, Suver et al. 2019). In flight however, wind only transiently activates mechanosensors (Fuller et al. 2014), but then displaces the fly as a whole, leading to an optic flow signal opposed to the fly's direction of movement (Kennedy et al. 1940, van Breugel et al. 2014). As different PFNs carry airflow and optic flow signals in a similar format (Lyu et al. 2020, Currier et al. 2020), this circuit may be well-poised to compute wind direction in both walking and flying flies. Separating the computation of stimulus value, in the MB/LH and tangential FB inputs, from the computation of wind direction, in PFNs, may allow flies to generalize stimulus associations learned in one context (walking) to another (flight).

Olfactory representations and circuits in the fan-shaped body

To our knowledge, the present study represents the first large-scale functional identification of olfactory neurons in the Cx. The olfactory FB tangential input lines that we identified here are distinct from those previously implicated in the regulation of sleep (Donlea et al. 2014), which produced distinct behavioral patterns (often slow walking) in our assay, although they may contain overlapping neurons. Importantly, we found that odor-responsive upwind-promoting tangential neurons innervate multiple layers of the FB, arguing against a model in which different FB layers encode different behavioral drives. Rather, our data suggest

a model in which different patterns of FB tangential neuron activation encode different behavioral states or needs, and lead to the selection of navigational motor programs through the activation of specific sets of FB local neurons. Exploring the activity of olfactory FB tangential neurons with a wider set of odor stimuli and behavioral states is likely to provide insight into how valence and behavioral state information is encoded across this population.

Although FB tangential inputs are morphologically similar to the tangential ring neurons that innervate the ellipsoid body, our investigation suggests that they exhibit very different physiology. While ring neurons are mostly inhibitory (Hulse et al. 2021) and exhibit strong spatial tuning for visual landmarks (Omoto et al. 2017, Fisher et al. 2019) and wind direction (Okubo et al. 2019), most of the FB tangential inputs we surveyed were excitatory, and showed spatially untuned responses to odor or wind. This difference in physiology may reflect a difference in function, where ring neurons provide landmark information that allows the fly to establish an estimate of allocentric heading (Seelig and Jayaraman 2015, Hulse et al. 2021), while FB tangential inputs may encode behavioral goals, needs, and states that allow the fly to select different navigational motor programs on a moment-to-moment basis (Sareen et al. 2021, LeMoël et al. 2019).

An intriguing feature of the circuit we identified is the presence of an excitatory input (FB5AB) onto the axon terminals of hΔC neurons, where we hypothesize that it might gate the output of these neurons ON during odor. Axo-axonic synapses appear to be widespread in the *Drosophila* brain (Schlegel et al. 2021) although most previously studied synapses of this type use inhibitory rather than excitatory gating (Root et al. 2008, Olsen et al. 2008). Whether FB5AB regulates hΔC activity solely through fast cholinergic excitation, or also through one of the many peptides and modulators expressed within the FB (Kahsai and Winther, 2010) remains to be determined. In this study we used connectomic approaches to identify one set of FB local neurons— hΔC neurons— that integrate wind and odor cues. However, it is likely that other FB local neurons also play a role in wind and odor integration. In our screen we identified several lines labeling predominantly local neurons that also promoted upwind movement (Fig. S3). Moreover, we identified multiple olfactory FB inputs that target different layers, likely synapsing on different sets of local neurons. Identifying which FB input neurons are labeled in each of the lines will be critical to uncovering the full complement of FB neurons that participate in olfactory navigation.

Here we showed that an attractive odor stimulus is broadly represented across the FB, and that many different populations of FB neurons promote upwind movement, indicating that the FB participates in olfactory navigation. However, it remains unclear whether all pathways involved in olfactory navigation run through the FB. Olfactory avoidance of geosmin has been shown to involve a direct pathway from the LH to descending neurons (Huoviala et al. 2020), while visual orientation to a female during courtship involves direct connections from visual interneurons to descending neurons (Ribeiro et al. 2018)— again bypassing the FB. In addition

to targeting the FB, MBONs also make direct connections to the lateral accessory lobe (LAL) a region implicated in motor control and steering (Namiki and Kanzaki, 2016, Rayshubskiy et al. 2020, Scaplen et al. 2021). As the LAL also receives wind direction input (Okubo et al. 2019), it could form a second site of wind and odor integration, that might operate in parallel with the circuit we have described through the FB. Finally, wind and odor signals may also be integrated close to the periphery, in the AMMC, WED, or antennal lobe, forming a more direct pathway from sensory input to motor output. In this study, we found that activation of FB neurons typically produced more persistent wind orientation phenotypes than activation of MB and LH output neurons. Thus, one possibility is that parallel pathways from olfactory centers to motor centers could regulate behavior on different timescales. Additionally, activity in the FB pathway might allow the fly to incorporate learning about its spatial environment into navigational decisions during food search. For example, FB circuitry might allow a fly to adopt courses at particular angles to the wind, in addition to directly up- or downwind, or it might allow the fly to generate an internal estimate of the direction of the odor source during plume navigation. Determining how activity in these different pathways shapes behavior on different timescales, and in different spatial contexts, will provide additional insight into the organization of central circuits for navigation.

Acknowledgements

The authors would like to thank Marc Gershow, Karla Kaun, Michael Dickinson, Michael Reiser, Matthew Clark, Matthieu Louis, Richard Mann, Gilad Barnea, Rachel Wilson, Tzumin Lee, Janelia Flylight, and the Bloomington and Vienna Drosophila Resource Centers for fly stocks. We thank Michael Long, Elizabeth Hong, Floris van Breugel, David Schoppik, and members of the Nagel and Schoppik labs for helpful input on the manuscript. This work was supported by R01DC017979, NSF Ideaslab (IOS-1555933) and NSF Neuronex grants, as well as a McKnight Scholar Award to K.I.N. M.H.S was supported by an NSF CAREER award IOS-204720. T.A.C was supported by a Dean's Dissertation Fellowship from NYU.

Author contributions:

K.I.N and A.M.M.M conceived the project, with a major conceptual contribution by A.J.L. A.M.M.M performed the vast majority of behavioral, imaging, electrophysiology, and anatomy experiments, and generated new genetic stocks. A.J.L. performed connectomic analysis and developed the computational model with input from K.I.N. and A.M.M.M. A.M.L. and A.J.L contributed to behavioral experiments. T.A.C. performed a subset of electrophysiology experiments. M.H.S. provided the genetic strategy to isolate Cx neurons. K.I.N, A.M.M.M, and A.J.L wrote the paper with input from the other authors.

Competing Interests: The authors declare no competing interests.

Methods

FLY STOCKS

All experimental flies (except trans-tango flies described below) were raised at 25° C on a standard cornmeal-agar medium. Flies were raised with a 12h light-dark cycle. We used the following genotypes and ages for the experiments shown in each figure. Parental genotypes and sources are listed in the Key Resources Table below. For optogenetic activation experiments, experiments were run in male norpA hemizygotes, which are genetically blind, to eliminate any possible innate visual responses to red light. All other flies used were female. We detected no difference in olfactory behavior of male versus female flies in our assay in a previous study (Alvarez-Salvado et al., 2018). For calcium imaging experiments we used older flies (5-21 days) to maximize indicator expression. For electrophysiology we used younger flies to minimize glial ensheathing which make it challenging to obtain clean patch recordings. Trans-tango flies were raised at 18°C and aged until they were 10-20 days old following recommended protocols (Talay et al., 2017).

Genotype	**Description**	**Age range**	**Figure panels**
Figure 1, S1			
norpA$_{36}$/y;UAS-Chrimson-mVenus/orco-GAL4;UAS-10xGFP/+	genetically blind male flies expressing Chrimson under the orco promoter	3-10 days	ACV experiments in Fig. 1C,D,E Fig S1A
norpA$_{36}$/y;tsh-gal80/orco-GAL4,IR8a-GAL4;UAS-Chrimson-mVenus/+	genetically blind male flies expressing Chrimson under the orco and IR8a promoters	3-10 days	Optogenetic activation experiments in Fig. 1C,D,E Fig. S1C
norpA$_{36}$/y;UAS-Chrimson-mVenus;UAS-10xGFP x X-GAL4 or split-GAL4 X-GAL4: orco-GAL4,IR8a-GAL4 (II), empty-GAL4 (II), empty split-GAL4 (II,III), OR59a (III), OR42a (III), IR75a (III), IR64a (II), OR92A (III), OR42b (II)	genetically blind hemizygous male flies expressing Chrimson under various GAL4 or split-GAL4 drivers on chromosomes II or III.	3-10 days	optogenetic activation experiments in Fig. 1E Fig. S1A,B,D
norpA$_{36}$/y;+/UAS-Chrimson-mVenus;+/UAS-10xGFP	parental control	3-10 days	parental control for activation in Fig. 1E

UAS-TNT$_{5905}$	parental control; UAS-TNT backcrossed 5 generations to w1118 5905	3-10 days	parental control for silencing in Fig. 1F
UAS-TNT$_{5905}$ x X-GAL4 X-GAL4: orco-GAL4, IR8a-GAL4, orco-GAL4,IR8a-GAL4	flies with various ORNs silenced	3-10 days	Fig. 1F,G, Fig. S1E
Figure 2, S2			
norpA$_{36}$/y;tsh-Gal80;UAS-Chrimson-mVenus x X-GAL4 or split-GAL4 X-GAL4/split-GAL4: LH1538, LH1396, LH1539, MB082C, MB077B, MB052B, MB434B, MB112C, MB011B, MB543B, MB050B, MB018B, MB027B, MB549C, LH2193, LH989, LH290.	genetically blind hemizygous male flies expressing Chrimson under various GAL4 or split-GAL4 drivers on chromosomes II or III. tsh-Gal80 included to suppress VNC expression.	3-10 days	Fig. 2A-D, Fig. S2A,B
UAS-TNT$_{5905}$ x X-GAL4 or split-GAL4 X-GAL4: LH1538, LH1396, LH1539, MB077B, MB052B, MB112C or + for parental control	flies with MB/LH neurons silenced	3-10 days	Fig. S1C
+;UAS-GCaMP6f;UAS-tdTomato x X-GAL4 X-GAL4: LH1396, MB052B, MB077B, MB082C, ss47432 (LNa)	GCaMP6f and tdTOM expressed in LHAd1b2 using the LH1396 split GAL4 driver or in MBONs15-19 using MB052B, MBON12 using MB077B, or MBON 13,14 using MB082C, LNa using ss47432	5-21 days	Fig. 2E, Fig. S2E
+;MB027B-GAL4AD/+;UAS-10xGFP/MB027B-GAL4DB	expression of GFP in ’3 MBONs for electrophysiology	1-3 days	Fig. 2F
Figure 3, S3			

UAS-myrGFP, QUAS-mtdTomato (3x HA); trans-Tango x X-GAL4 X-GAL4: LH1396, MB052B	Trans-tango driven by LH1396 and MB052B	10-20 days; raised at 19°C	Fig. 3A
norpA$_{36}$/y;tsh-Gal80;UAS-Chrimson-mVenus x X-GAL4 or split-GAL4 Dorsal Inputs: VT056792-GAL4, VT002458-GAL4, 84C10-GAL4, VT027955-GAL4, 58F01-GAL4, 58F02-GAL4, 71A02-GAL4,VT026663-GAL4, VT20633-GAL4, VT004849-GAL4, 23E10-GAL4, 26B11-GAL4, 28H10-GAL4, 12D12-GAL4, 65C03-GAL4, 45D04-GAL4, LH2392 Ventral Inputs: VT036875-GAL4, 33E06-GAL4, VT056509-GAL4, 72A04-GAL4, 78G09-GAL4, vt049652-GAL4, 13B10-GAL4, VT033929-GAL4, VT046276-GAL4, VT041421-GAL4,VT029515-GAL4 PFN: 44B10-GAL4; VT039497-GAL4,16D01-GAL4, 67B06-GAL4, SS52577, SS52244, SS54549, SS02255, SS00239, 43D09AD; VT000986DB Split-GAL4: 43D09-AD;65C03-DB, 12D12-AD;VT027955-DB, VT026663AD;65C03DB, 12D12AD;65C03DB, VT041421AD;28H10DB, VT041421AD;33E06DB, VT041421DB;65H10DB, VT029515AD; 78G09DB, LH1478, 13B10AD;VT029515DB, 13B10AD; VT041421DB	genetically blind hemizygous male flies expressing Chrimson under various GAL4 or split-GAL4 drivers on chromosomes II or III. tsh-Gal80 included to suppress VNC expression.	3-10 days	Fig. 3B, C, S3

Blank: Empty-GAL4, Empty Split-Gal4			
norpA$_{60}$/y;tsh-Gal80;UAS-Chrimson-mVenus x X-GAL4 or split-GAL4 Additional Cx neurons: 19C06-GAL4, 65H10-GAL4, VT024599-GAL4, VT058487-GAL4, VT000986-GAL4, 24E05-GAL4, VT062617-GAL4, 43D09-GAL4, VT019352-GAL4, VT030322-GAL4, 94G02-GAL4, VT050238-GAL4, VT063191-GAL4, VT060736-GAL4, 43D09AD;VT062617DB, VT063948-GAL4, 46G06-GAL4, V000624-GAL4, VT060202-GAL4, 73A06-GAL4, VT037489-GAL4, VT020739-GAL4, VT032906-GAL4, 60D05-GAL4, SS50464, SS02718, SS50420			
Figure 4, S4			
CLIN x UAS-Chrimson-mVenus;21D07-GAL4	21D07>Chrimson-mVenus filtered through CLIN to restrict expression to type II (Cx) neurons	3-10 days	Fig. 4A (anatomy),C (behaviour) Fig. S4A
+;UAS-GCaMP6f;UAS-tdTomato x X-GAL4 X-GAL4: 21D07-GAL4, 65C03-GAL4, vFB split (13B10AD;VT041421DB), 12D12-GAL4	GCaMP6f and tdTOM expressed under the various FB drivers	5-21 days	Fig. 4B,D imaging, Fig. S4D,E
+;UAS-GCaMP6f;UAS-tdTomato x X-GAL4 X-GAL4: MB052B, MB077B, MB082C, lh1386,21D07-GAL4, 65C03-GAL4, vFB split (13B10AD;VT041421DB), 12D12-GAL4	GCaMP6f and tdTOM expressed under the various drivers	5-21 days	Fig. 4E

norpA$_{36}$/y;tsh-Gal80;UAS-Chrimson-mVenus x X-GAL4 or split-GAL4 X-GAL4: 65C03-GAL4, 12D12-GAL4, vFB split (13B10AD;VT041421DB), VT029515-GAL4	genetically blind hemizygous male flies expressing Chrimson under various GAL4 or split-GAL4 drivers on chromosomes II or III. tsh-Gal80 included to suppress VNC expression.		Fig. 4A (anatomy),C (behavior), Fig. S4A
UAS(FRT.stop)-Chrimson-mVenus; LexAop-FLP; ChAT-LexA; ChAT-LexA x X-GAL4 or split-GAL4 X-GAL4: 21D07-GAL4, 65C03-GAL4, vFB split (13B10AD;VT041421DB)	cross to identify cholinergic neurons within a GAL4 or split-GAL4 line	3-20 days	Fig. S4B
UAS(FRT.stop)-Chrimson-mVenus; LexAop-FLP; Gad1-LexA x X-GAL4 or split-GAL4 X-GAL4: 65C03-GAL4	cross to identify GABAergic neurons within a GAL4 or split-GAL4 line	3-20 days	Fig. S4B
UAS-TNT$_{IMS}$ x X-GAL4 or split-GAL4 X-GAL4: 65C03-GAL4, 45D04-GAL4, VT029515-GAL4, vFB split (13B10AD;VT041421DB)	flies with FB neurons constitutively silenced	3-10 days	Fig. S4C
norpa^{36}/+;s/+;X-GAL4/UAS-GTACR1 or norpa^{36}/+;s/X-GAL4; UAS-GTACR1/+X-GAL4(II): orco-GAL4, IR8a-GAL4X-GAL4(III): 21D07-GAL4, VT062617-GAL4	Flies with FB neurons temporally silenced	3-10 days	Fig. S4C
Figure 5, S5			
+;UAS-GCaMP6f;UAS-tdTomato x VT062617-GAL4	GCaMP6f and tdTOM expressed in hΔC neurons	5-21 days	Fig. 5D-H, S5A
norpA$_{36}$/y;tsh-Gal80;UAS-Chrimson-mVenus x X-GAL4 or split-GAL4	genetically blind hemizygous male flies expressing Chrimson under various GAL4 or split-GAL4 drivers		Fig. 5I, S5C

X-GAL4: VT062617-GAL4, hΔC split1 (19G02AD;VT062617DB), hΔC split2 (VT024634AD; VT062617DB)	on chromosomes II or III. tsh-Gal80 included to suppress VNC expression.		
UAS(FRT.stop)-Chrimson-mVenus; LexAop-FLP; ChAT-LexA; ChAT-LexA x VT062617-GAL4	cross to identify cholinergic neurons within a GAL4 line	3-20 days	Fig. S5B
UAS(FRT.stop)-Chrimson-mVenus; LexAop-FLP; Gad1-LexA x VT062617-GAL4	cross to identify GABAergic neurons within a GAL4 line	3-20 days	Fig. S5B
Figure 6, S7			
norpA^{36}/y;UAS-Chrimson-mVenus/orco-GAL4;UAS-10xGFP/+	genetically blind male flies expressing Chrimson under the orco promoter	3-10 days	ACV experiments in Fig. 6C,D, S7A

BEHAVIORAL EXPERIMENTS

For behavioral experiments we used a modified version of the miniature wind tunnel setup described in Alvarez-Salvado et al. 2018. Briefly, flies were constrained to walk in a shallow arena with constant laminar airflow at 11.9 cm/s and tracked using IR LEDS (850nm, Environmental Lights) and a camera (Basler acA1920-155um). In experiments with odor, a 10s pulse of 1% apple cider vinegar (Pastorelli) was introduced through solenoid valves located immediately below the arena. For optogenetic activation experiments, we used red LEDs (626nm, SuperBrightLEDS), interleaved with the IR LEDs in a panel positioned 4.5cm above the arena. Light intensity was measured with a light meter (Thorlabs) and was 26 uW/mm, measured at 626nm, for the majority of activation experiments. In flies expressing Chrimson using the CLIN technique the light level was 34 uW/mm (Aso et al., 2014) to compensate for low Chrimson expression in this line. For optogenetic silencing experiments, light panels with blue LEDs (470nm, Environmental Lights), were used. Light intensity for silencing experiments was 58 uW/mm, measured at 530nm. Wind and odor stimuli were calibrated using a hotwire anemometer (Dantec Instruments) and photo-ionization detector (miniPID, Aurora Systems) respectively.

Flies (males or mated females) were collected 2 to 7 days before the experiment and housed in time shifted boxes on 12h cycles. For optogenetic experiments, flies were placed on cornmeal-agar food supplemented with 50uL all-trans retinal (35mM stock: Sigma, R2500, dissolved in ethanol, stored at -20°C) mixed into ~1 teaspoon of hydrated potato flakes. These

vials were covered with aluminum foil except for a small window near the fly plug. All flies began the experiment (~1.5-2h) between their subjective ZT1 and ZT4. 20-24h before the experiment we deprived flies of food by placing them in a polystyrene vial with damp shredded kimwipe. Flies were briefly anaesthetized by placing the vial on ice for ~1min before loading into the arena. Flies were allowed 5-10 minutes to recover before the experiment began. Flies for genetic silencing were run in the dark, while optogenetic activation experiments were run with ambient lighting. During experiments with odor, flies received blocks of three trial conditions in random order: wind and odor (30s wind alone, 10s odorized air, 30s wind alone), wind alone (70s), or no wind (70s). During optogenetic activation experiments, flies received blocks of four trial conditions in random order: light stimulation with wind (30s wind, 10s wind and light, 30s wind), light stimulation alone (30s no stimulus, 10s light, 30s no stimulus), wind alone (70s wind), or blank trials (70s).

We analyzed behavioral data in a similar fashion as in Alvarez-Savaldo et al. 2018. X,Y coordinates and orientation were tracked in real time at 50Hz using custom Labview software (National Instruments). Data were further analyzed offline using custom MATLAB scripts. Coordinates and orientation were low-pass filtered at 2.5Hz using a 2-pole Butterworth filter. Any trials with tracking errors, or where the fly moved less than 25mm overall were discarded from further analysis. Any fly which moved on less than 5 trials for a condition was excluded as well. For all measured parameters (see below) time periods when the fly was stationary (moving at less than 1mm/s) were omitted. In trials with odor stimuli, we aligned the time courses of behavioral parameters to the actual time the fly encounters the odor based on their position is the arena, based on delays recorded by miniPID.

Behavioral parameters as a function of time were calculated as follows for each trial: Distance moved was calculated as the length of the hypotenuse between two pairs of coordinates at each frame. Groundspeed was calculated as the distance moved divided by the time interval of a frame (20ms). Upwind velocity was calculated as the change in Y-coordinates divided by the frame interval. Angular velocity was calculated as the absolute value of the change in unwrapped orientation divided by the time frame interval. Curvature was calculated as the filtered angular velocity divided by the filtered groundspeed. Probability of movement (pmove) was calculated by binarizing groundspeed with a threshold of 1 mm/s.

Quantification of average behavioral parameters represent average parameters across trials for each fly. All parameters were compared to a baseline period (10-25s in the trial) expect place preference where the baseline was taken from 25-30s into the trial (immediately before stimulus onset at 30s). We used the following time windows for analysis: probability of movement (pmove): 0-5s from stimulus onset, upwind velocity (upwind): 0-5s from stimulus onset for periphery, LH, MB, 0-10s from stimulus onset for FB, offset upwind velocity (upwindoff): 0-2s after stimulus offset, groundspeed: 2s-5s from stimulus onset, offset groundspeed: 0-2s after stimulus offset, angular velocity (angv): 2s-5s from stimulus onset, offset angular velocity (angvoff): 0-2s after stimulus offset, onset angular velocity (angvon): 0-1s

from stimulus onset, curvature: 2s-5s from stimulus onset, offset curvature (curvatureoff): 0-2s after stimulus offset, onset curvature (curvature on): 0-1s from stimulus onset, place preference (placepref): 7.5s from stimulus onset to 2.5s after stimulus offset. For display purposes we do not depict the significance values in tables (Fig 3. B,C, Fig S3) for upwind velocity for small magnitude increases (<1mm/s). We do not display values for curvature (both stimulation and offset) if angular velocity is below <50deg/s and groundspeed is <4mm/s. We excluded these values because the curvature increase was due mostly to the drop in groundspeed and trajectories in these cases did not exhibit the characteristics of search. To examine the persistence of upwind displacement we looked at the change in displacement relative to position at stimulus offset (Fig 3F). We averaged this across trials for individual flies, and averaged across flies for 10s following stimulus offset for the depiction in the figure.

CALCIUM IMAGING

For calcium imaging experiments, flies were cold-anaesthetized and mounted in a version of the fly holder described in Suver et al. 2019. The fly's head was positioned in a keyhole shaped metal cutout (etchit) within a plastic holder. We attached the fly to the holder using UV glue (Riverruns UV clear Glue, thick formula), and stabilized the proboscis to the head/body, leaving the antenna free to move. We removed the front two legs to prevent interference with airflow stimuli. Under *Drosophila* extracellular saline (103 mM NaCl, 3 mM KCl, 5 mM TES, 8 mM trehalose dihydrate, 10 mM glucose, 26 mM NaHCO3, 1 mM $NaH_2PO_4H_20$, 1.5 mM $CaCl_22H_2O$, and 4 mM $MgCl_26H_2O$, pH 7.1-7.4, osmolarity 270-274 mOsm), we dissected away the cuticle at the back of fly's head using fine forceps. We removed the trachea, airsacs, and muscle over the surface of the brain. Flies were starved for 18-24h prior to the experiment. External saline bubbled with carbogen (5% CO_2, 95% O_2) was perfused for the duration of the experiment.

2-Photon imaging was performed using a pulsed infrared laser (Mai Tai DeepSea, Spectraphysics) with a Bergamo II microscope (Thorlabs). Images were acquired through a 20x water immersion objective (Olympus XLUMPLFLN 20x) using ThorImage 3.0 software. The wavelength of the laser was set to 920 nm and power at the sample ranged from 13 to 66mW. Spectral separation of emitted photons was accomplished with two bandpass filters (red, tdTOM, 607/70nm, green, GCamp6f, 525/50nm) and detected by GaAsP PMTs. Imaging areas varied depending on the genotype but were between 47 x 47uM and 122 x 74uM. Imaging regions were identified first using the tdTOM signal under epifluorescence. Images were acquired at ~5.0 frames per second. Across genotypes we excluded any flies where we were unable to obtain 5 trials of each direction, either due to fat migration or cell death. We excluded 2 flies from the 65C03-GAL4 data which showed rhythmic spike like activity and did not respond to any phase of our stimulus. For VT062617-GAL4 imaging we excluded 1/17 flies as no columns showed had an average response >2STD above baseline.

The majority of airflow and odor stimuli were delivered using a 5-direction manifold described in Suver et al. 2019 and Currier et al. 2020. Air was charcoal filtered, then passed through a flowmeter (Cole-Parmer), and proportional valves (EVP series, EV-05-0905; Clippard instruments laboratory,Cincinnati, OH) to direct air or odorized air at the fly from one of 5 directions. Airspeed was ~25cm/s. For a small subset of additional experiments, we used a stepper motor (Oriental motor, PKP564FMN24A) and rotary union (DSTI, LT-2141) to rotate airflow and odor stimuli around the fly, while the fly remained stationary in the center of the arena (Currier et al., 2020). In these experiments we rotate the stimulus to the same 5 directions we could present with the manifold. Airspeed was 40 cm/s and presented through 3-way solenoid valves (Lee Company, LHDA1233115HA). We used a hotwire anemometer (Dantec Instuments) to verify that airspeed was equivalent across directions and constant through the wind and odor phases of the stimulus. Odorant (apple cider vinegar, 10%) was diluted in distilled water on the day of the experiment. Each trial consisted of 5-10s without stimuli, 10s of wind alone, 10s of odorized wind, 10s of wind alone and 8-10s of no stimulus following the wind. We randomized the direction from which odor was presented in blocks of 5 trials and completed 5 blocks for each fly (25 total trials). We adjusted imaging position, Z-plane, gain, and power levels after each block as necessary. Of the flies included, we present data from all 25 trials here. MB052B, LH1396, 65C03-GAL4, 21D07-GAL4, vFB split, and VT062617-GAL4 were imaged with the stimulus manifold, while MB077B, MB082C and 12D12-GAL4 were imaged with the rotating stimulus setup. Stimuli were controlled through custom MATLAB and Python scripts.

Analysis of calcium data was performed as in Currier et al. 2020. We used the CalmAn MATLAB package, ImageJ, and custom MATLAB scripts to align and analyze data. We used the CalmAn package (Giovannucci et al. 2019) to implement the NoRMCorre rigid motion correction algorithm (Pnevmatikakis et al. 2017) on the red (tdTOM) time series and applied the same shifts to the green (GCaMP6f) times series. We drew regions of interest (ROIs) by hand on maximum intensity projections of the tdTom time series for the first trial. ROIs were applied to all trials, and had their position manually adjusted using imageJ if significant drift occurred between trials. ROIs were drawn around the following regions: for LH1396, the ROI was placed around the dendritic processes in the LH, for MB052B, MB082C and MB077B the ROIs were placed around the putative axonal processes in the protocerebrum. ROI location and imaging region was selected based on pilot experiments recording from different planes and ROIs. For tangential FB inputs (FB5AB, 65C03-GAL4, 12D12-GAL4 and vFB split) we imaged from the FB layer innervated by each GAL4 line. We report imaging quantifications across the entire layer in the figures. In tangential inputs we did not observe obvious direction specific responses in different anatomical locations of the output layer. For VT062617-GAL4 imaging of hΔC neurons, we drew ROIs across 8 putative columns of the FB based on the glomerular structure that was observable in the tdTom signal. In some cases, the true number of columns was unclear and depended on the exact plane of imaging and positioning of the fly's head. ImageJ ROIs were imported into MATLAB using ReadImageJROI (Muir et al. 2014). We calculated ΔF/F for the GCaMP6f time series by dividing the time series by the average fluorescence of the baseline period (first 5s of the trial, excluding the first sample due to shutter lag). For main text figures

we present the average ΔF/F signal for individual flies. Mean traces were calculated by resampling to 5 samples per second if frame rate varied between experiments. Supplemental figure heat maps were normalized to maximum response across all trials within an individual fly.

ELECTROPHYSIOLOGY

We performed whole cell patch clamp recordings as described previously (Suver et al. 2019, Currier et al. 2020). Mounting and dissection were similar to that described above for calcium imaging, except that we used hot wax rather than UV glue to fix the fly in place. In addition, we removed the sheath covering the brain using collagenase (5% in extracellular saline, Worthington Biochemical Corporation Collagenase Type 4) under positive pressure applied with a fine tipped electrode (5-10uM diameter). Cell bodies of interest were visualized with 10x cytoplasmic GFP using an LED source (Cairn Research MONOLED) and filter cube (U-N19002 AT-GFP/F LP C164404). Brains were visualized under 40x magnification (Olympus, LUMPLFLN40XW) using a camera (Dage-MTI, IR-1000) and an LCD monitor (Samsung, SMT-1734). Cell bodies were cleaned using external saline and positive pressure, as well as light negative pressure to remove cell bodies near our cell of interest.

For whole-cell patch clamp recordings, we pulled 6 to 10 M-Ohm glass pipettes made of thick-walled glass (World Precision Instruments 1B150F-3) using a Sutter Instruments P-1000 puller. Pipettes were polished using a pressurized micro-forge (Scientific Instruments, CPM-2). Our intracellular solution contained 140 mM KOH, 140 mM aspartic acid, 10 mM HEPES, 1 mM EGTA, 1 mM KCl, 4 mM MgATP, 0.5 mM Na3GFP, and 13 mM biocytin hydrazide (for visualization of neural processes). Current and voltage signals were amplified using either an A-M systems Model 2400 amplifier or a Molecular Devices Multiclamp 700B. Recordings acquired with the A-M systems amplifier were paired with additional preamplification using a Brownlee Precision 410 preamplifier. We controlled stimuli and hardware using custom MATLAB and Arduino software scripts. All electrophysiological recordings were acquired at 10kHz.

Stimuli were delivered using an olfactometer similar to the one described in Nagel and Wilson 2016. Charcoal-filtered air was passed through a flowmeter (Cole-Parmer, 0.3 L/min), and then split into two airstreams that passed over either odorant (10% ACV) or water. These two airstreams were then passed through two three-way solenoid valves (Lee company, LFAA1201610H) that allowed a signal to switch which airstream (odor or water) was directed into the main airflow. Main airflow (1L/min) was delivered to the fly through a Teflon tube (4mm outer diameter, 2.5mm inner diameter). The Teflon tube was positioned <1mm from the head of the fly using a micro manipulator for each experiment using two cameras (Unibrain). The airflow delivery system was positioned on the right side of the fly, thus cells on the fly's right were ipsilateral while those on the left were contralateral. Pulses of 2s, 10s or 20s of odor were presented to the fly. Only 10s of ACV is displayed here.

We used custom MATLAB scripts to analyze electrophysiology data. To analyze membrane potential, we applied a 2.5Hz Butterworth filter to remove spikes. We averaged the baseline period of of 2s and subtracted this from the average time course for each fly for presentation purposes. We report the difference between the baseline period (wind only) and the average during the first 4s of the odor period. The resting potential varied between (-34.6 mV and -25.2 mV for MBONs α'3). The average resting potential was: -30.8mV. We recorded from a total of 12 MBONs, 6 on each side that met our criteria for quality of recording based on input to access ratio great than 5:1.

IMMUNOHISTOCHEMISTRY

We performed immunohistochemistry as in previous reports (Suver et al. 2019, Currier et al. 2020). We fixed brains for 15 minutes in 4% paraformaldehyde (in 1X phosphate buffered saline, PBS). Next, we washed the brain three times in PBS and stored at 4°C until antibody staining (immediately or within 2 weeks). We incubated brains in a blocking solution containing 5% normal goat serum dissolved in PBST (1x PBS with 0.2% Triton-X) for 20-60 minutes. Brains were incubated at room temperature in a solution of primary antibodies (see below for exact components). We then washed brains three times in PBST and incubated brains in a secondary antibody solution at room temperature for 24h. We washed brains three times in PBST and then stored in PBS at 4°C until imaging. To mount brains for imaging we placed brains in vectashield (Vector Labs H-1000) and sealed with coverslips and nail polish. We imaged brains at 20x magnification of a Zeiss LSM 800 confocal microscope with a 20x objective (Zeiss W Plan-Apochromat 20x/1.0 DIC CG 0.17 M27 75mm). All brains were imaged at 1-1.25uM depth resolution. Final images are presented as maximum Z projections over relevant depths.

To visualize the expression of *Chrimson-mVenus* in driver lines used for optogenetic activation experiments, we dissected brains of females from the same cross as experimental males. We visualized 1-3 brains for each genotype (data not shown) to assess the breadth of expression under the Chrimson effector.

We used the following antibody mixes for the experiments listed: Chrimson/neurotransmitter stains: primary: chicken anti-GFP (1:50) & mouse anti-nc82 (1:50); secondary: anti-chicken Alexa488 (1:250) & anti-mouse Alexa 633 (1:250). Electrophysiology stains: primary: chicken anti-GFP (1:50) & mouse anti-nc82 (1:50); secondary: anti-chicken Alexa488 (1:250), anti-mouse Alexa 633 (1:250) and Alexa568-conjugated streptavidin (1:1000). Trans-tango and CLIN stains: primary: chicken anti-GFP (1:50), mouse anti-nc82 (1:50), & rabbit anti-dsRed (1:500); secondary: anti-chicken Alexa 488 (1:250), anti-mouse Alexa 633 (1:250) and anti-rabbit Alexa 568 (1:250). GABA stains: chicken anti-GFP (1:50),

mouse anti-nc82 (1:50) & rabbit anti-GABA (1:100); anti chicken Alexa488 (1:250), anti-mouse Alexa 633 (1:250) & anti-rabbit Alexa 568 (1:250).

CONNECTOMIC ANALYSIS

Data from the hemibrain connectome (Scheffer et al. 2020) were interpreted using neuprint explorer (neuprint.janelia.org, version d2a8f5785d73421096f7cdc09ad585e5). Further analysis and visualization were completed using custom MATLAB and Python scripts. For the analysis shown in Fig. 5B, the location of FB5AB synapses onto hΔC was determined by their x position. No filtering or constraints were applied in synapse counts for this panel. For the analysis in Fig. 4B, we counted all FB tangential neurons two synapses downstream of the following projection neurons: VM7d_adPN, VM7v_adPN, DM1_lPN, DM4_adPN, DM4_vPN, VA2_adPN, DP1l_adPN, DP1l_vPN, DL2d_adPN, DL2d_vPN, DL2v_adPN, DC4_adPN, DC4_vPN, DP1m_adPN, DP1m_vPN in which the intermediate neurons contained LH (they were lateral horn neurons) and where synaptic weights exceeded a weight of 3.

MODELING

FB heading bumps were simulated in wind-sensitive PFNs, PFL3, and PFL2 populations using one-cycle sinusoids defined by:

$$activity = \cos(FB_{location} - (180° - heading + shift))*scale$$

Where $FB_{location}$ refers to the spatial location within the FB (0° = left FB, 360° = right FB), *heading* refers to the heading direction of the fly, *shift* refers to the phase shift introduced by a given cell type, and *scale* refers to the sinusoid amplitude. The shift parameters were taken directly from the connectome (Hulse et al. 2021), and were defined as the following: $shift_{left_PFN}$ = +45°, $shift_{right_PFN}$ = -45°, $shift_{left_PFL3}$ = -90°, $shift_{right_PFL3}$ = +90°, $shift_{left_PFL2}$ = -180, $shift_{right_PFL3}$ = +180°. The scale parameters were equal to 1 for all cell types except PFNs, which instead varied with wind direction according to the following sinusoid equation:

$$scale_{windPFN} = \sin((heading - wind) + (90° - peak))$$

Where *heading* refers to the heading direction of the fly, *wind* refers to the allocentric wind direction, and *peak* refers to the egocentric wind direction that maximally activates the PFN cell type ($peak_{left_PFN}$ = -45°, $peak_{right_PFN}$ = +45°).

To predict turning via the direct and indirect pathways, the heading bumps in PFN populations were shifted (0° for direct pathway, 180° for indirect pathway), added to the heading

bumps in left and right PFL3 populations, and then the amplitudes of the resulting sinusoids (one for left PFL3 and one for right PFL3) were compared:

$$\%RightPFL3_{dir} = max(PFL3_{right} + PFN_{right} + PFN_{left})/[max(PFL3_{right} + PFN_{right} + PFN_{left})+max(PFL3_{left} + PFN_{right} + PFN_{left})]*100\%$$

$$\%RightPFL3_{indir} = max(PFL3_{right} - (PFN_{right} + PFN_{left}))/[max(PFL3_{right} - (PFN_{right} + PFN_{left}))+max(PFL3_{left} - (PFN_{right} + PFN_{left}))]*100\%$$

To predict forward velocity via the direct and indirect pathways, the heading bumps in PFN populations were shifted (0° for direct pathway, 180° for indirect pathway), added to the heading bump in the left and right PFL2 population, and then the amplitude of the resulting sinusoid was computed. We doubled the amplitude to indicate that this process happens twice, once for left PFNs and once for right PFNs:

$$PFL2_{dir} = 2 * max(PFL2 + PFN_{right} + PFN_{left})$$

$$PFL2_{indir} = 2 * max(PFL2 - (PFN_{right} + PFN_{left}))$$

QUANTIFICATION AND STATISTICAL ANALYSIS

Behavior: Based on previous analysis of behavioral data (Alvarez-Salvado et al. 2018, Suver et al. 2019) we assumed behavioral data was not normally distributed. We applied non-parametric statistics to compare results and corrected for multiple comparisons using the Bonferroni method. We used the two-sided Wilcoxon signed rank test (MATLAB signrank) to compare the average baseline value of each parameter to the average of the parameter over a window of interest. Between genotype comparisons (genetic silencing experiments) were made between baseline subtracted parameter values using the two-sided Mann-Whitney U test (MATLAB ranksum). For behavioral time courses we display standard error around the mean. For summary plots we present standard deviation around the mean. Bonferroni corrections were applied based on the number of genotypes tested labelling similar neuron types (i.e. 6 in Fig. 1D, 21 for all dorsal FB inputs in Fig. 3B,C) or for the number of comparisons made to control in genetic silencing experiments (3 in Fig. 1F).

Imaging and physiology: We used parametric tests for calcium imaging and electrophysiological data. When testing for significant differences in odor responses across directions we averaged individual trials across flies, and performed a one-way ANOVA across pooled trials across flies (MATLAB anova1). When assessing differences between wind onset responses and odor responses we calculated mean wind and odor responses in 10s windows following onset. We compared wind and odor periods using a two-tailed paired student's t-test (MATLAB ttest, Fig. S4E, Fig. S5A). Similarly, we performed two-tailed paired student's t-test

when comparing wind and odor responses in MBON electrophysiology experiments and an two-tailed unpaired student's t-test (MATLAB ttest2) when comparing odor responses between ipsilateral and contralateral MBONs. To assess the decay (Fig 4D) of the fluorescence response to odor over time, we computed the average response to the odor presentation period across flies for five trial blocks, including one trial of each direction. We averaged the response across all flies imaged, and normalized by the mean response in trial block one. Shaded regions depict standard error across flies around the mean. We computed the tuning index (Fig 2E, 4E) as the difference between the average response to -90 and 90 for each fly. We used the odor period for all lines, except LNa, as responses were strongest to wind onset and not significantly modulated by odor (Currier et al., 2020). Error bars represent standard deviation of the mean.

KEY RESOURCES TABLE

Resource	Source	Identifier
antibodies		
chicken anti-GFP	Fisher Scientific	RRID:AB_1074893
mouse anti-nc82	DSHB	RRID:AB_2314866
rabbit anti-DsRed	Clontech	632496
Rabbit anti-GABA	Sigma	RRID:AB_477652
Alexa488-conjugated goat anti-chicken	Fisher Scientific	RRID:AB_2534096
Alexa633-conjugated goat anti-mouse	Fisher Scientific	RRID:AB_2535719
Alexa568-conjugated goat anti-rabbit	Fisher Scientific	RRID:AB_2315774
Alexa568-conjugated streptavidin	Fisher Scientific	RRID:AB_2576217
chemicals		
apple cider vinegar	Pastorelli	
experimental models: organisms/strains		
D. mel: orco-GAL4 (backcrossed into *w118* 5905)	BDSC	RRID:BDSC_26818
D. mel: OR59a-GAL4 (III)	BDSC via Marc Gershow	RRID:BDSC_9990
D. mel: OR42b-GAL4 (II)	BDSC via Marc Gershow	RRID:BDSC_9971
D. mel: OR42a-GAL4 (III)	BDSC	RRID:BDSC_9969
D. mel: IR75a-GAL4/TM6B	BDSC	RRID:BDSC_41748
D. mel: IR64a-GAL4;TM2/TM6	BDSC	RRID:BDSC_41732
D. mel: OR92a-GAL4	BDSC	RRID:BDSC_23139

D. mel: IR8a-GAL4;TM2/TM6	BDSC	RRID:BDSC_41731
D. mel: 60D05-GAL4	BDSC	RRID:BDSC_39247
D. mel: 46G06-GAL4	BDSC	RRID:BDSC_41271
D. mel: 44B10-GAL4	BDSC	RRID:BDSC_50202
D. mel: 16D01-GAL4	BDSC	RRID:BDSC_48722
D. mel: 19C06-GAL4	BDSC	RRID:BDSC_48843
D. mel: 67B06-GAL4/TM3	BDSC	RRID:BDSC_48294
D. mel: 73A06-GAL4	BDSC	RRID:BDSC_39805
D. mel: 84C10-GAL4	BDSC	RRID:BDSC_48378
D. mel: 71A02-GAL4	BDSC	RRID:BDSC_39560
D. mel: 23E10-GAL4	BDSC	RRID:BDSC_49032
D. mel: 26B11-GAL4	BDSC	RRID:BDSC_49164
D. mel: 28H10-GAL4	BDSC	RRID:BDSC_48085
D. mel: 12D12-GAL4	BDSC	RRID:BDSC_48506
D. mel: 65C03-GAL4	BDSC	RRID:BDSC_41290
D. mel: 45D04-GAL4	BDSC	RRID:BDSC_48160
D. mel: 65H10-GAL4	BDSC	RRID:BDSC_49614
D. mel: 43D09-GAL4	BDSC	RRID:BDSC_49553
D. mel: 24E05-GAL4	BDSC	RRID:BDSC_49081
D. mel: 94G04-GAL4	BDSC	RRID:BDSC_40699
D. mel: 33E06-GAL4	BDSC	RRID:BDSC_48114
D. mel: 72A04-GAL4	BDSC	RRID:BDSC_46665
D. mel: 78G09-GAL4	BDSC	RRID:BDSC_40015
D. mel: 13B10-GAL4	BDSC	RRID:BDSC_48548
D. mel: 21D07-GAL4	BDSC	RRID:BDSC_48943
D. mel: 58F01-GAL4	BDSC	RRID:BDSC_48213
D. mel: 58F02-GAL4	BDSC	RRID:BDSC_39186
D. mel: empty GAL4	BDSC	RRID:BDSC_68384
D. mel: empty split GAL4	BDSC	RRID:BDSC_79603
D. mel: 43D09AD	BDSC	RRID:BDSC_70691
D. mel: VT000986DB	BDSC	RRID:BDSC_75369
D. mel: VT026663AD	BDSC	RRID:BDSC_73054
D. mel: 12D12DB	BDSC	RRID:BDSC_69213
D. mel: VT027955DB	BDSC	RRID:BDSC_73229
D. mel: 65C03DB	BDSC	RRID:BDSC_69323
D. mel: 65C03AD	BDSC	RRID:BDSC_71005
D. mel: 45D04-DB	BDSC	RRID:BDSC_69239
D. mel: 12D12AD	BDSC	RRID:BDSC_70539
D. mel: VT041421AD	BDSC	RRID:BDSC_71457
D. mel: 28H10DB	BDSC	RRID:BDSC_69496
D. mel: 33E06DB	BDSC	RRID:BDSC_69229
D. mel: 65H10DB	BDSC	RRID:BDSC_86702
D. mel: VT029515AD	BDSC	RRID:BDSC_74286

D. mel: 78G09DB	BDSC	RRID:BDSC_69718
D. mel: 13B10AD	BDSC	RRID:BDSC_68828
D. mel: VT029515DB	BDSC	RRID:BDSC_75470
D. mel: VT041421DB	BDSC	RRID:BDSC_73472
D. mel: VT063948-GAL4	VDRC	VDRC: 200657
D. mel: VT000624-GAL4	VDRC	VDRC: 202720
D. mel: VT060202-GAL4	VDRC	VDRC: 202779
D. mel: VT037489-GAL4	VDRC	VDRC: 206278
D. mel: VT020739-GAL4	VDRC	VDRC: 201501
D. mel: VT032906-GAL4	VDRC	VDRC: 202537
D. mel: VT039497-GAL4	VDRC	VDRC: 205730
D. mel: VT056792-GAL4	VDRC	VDRC: 206056
D. mel: VT002458-GAL4	VDRC	VDRC: 202329
*D. mel: VT*027955-GAL4	VDRC	VDRC: 202476
D. mel: VT026663-GAL4	VDRC	VDRC: 203208
D. mel: VT020633-GAL4	VDRC	VDRC: 207839
D. mel: VT004849-GAL4	VDRC	VDRC: 207295
D. mel: VT024599-GAL4	VDRC	VDRC: 202132
D. mel: VT058487-GAL4	VDRC	VDRC: 207739
D. mel: VT062617-GAL4	VDRC	VDRC: 206875
D. mel: VT000986-GAL4	VDRC	VDRC: 207036
D. mel: VT019352-GAL4	VDRC	VDRC: 201718
D. mel: VT030322	VDRC	VDRC: 204795
D. mel: VT050238-GAL4	VDRC	VDRC: 201475
D. mel: VT063191-GAL4	VDRC	VDRC: 205643
D. mel: VT060736-GAL4	VDRC	VDRC: 202781
D. mel: VT036875-GAL4	VDRC	VDRC: 203402
D. mel: VT056509-GAL4	VDRC	VDRC: 201744
D. mel: VT049652-GAL4	VDRC	VDRC: 204721
D. mel: VT033929-GAL4	VDRC	VDRC: 206842
D. mel: VT046276-GAL4	VDRC	VDRC: 207814
D. mel: VT041421-GAL4	VDRC	VDRC: 200867
D. mel: VT029515-GAL4	VDRC	VDRC: 204785
D. mel: LH1396	Janelia	Janelia: 3026621
D. mel: LH1538	Janelia	Janelia: 3024098
D. mel: LH1539	Janelia	Janelia: 3024933
D. mel: LH989	Janelia	Janelia: 3032170
D. mel: LH290	Janelia	Janelia: 2502068
D. mel: LH2392/CyO;TM6	Janelia	Janelia: 3024051
D. mel: LH1478/CyO;TM6	Janelia	Janelia: 3032196
D. mel: LH2193	Janelia	Janelia: 3024119
D. mel: MB052B	Karla Kaun	
D. mel: MB077B	Karla Kaun	Janelia: 2135209

D. mel: MB543B	Karla Kaun	Janelia: 2501888
D. mel: MB050B0	Karla Kaun	Janelia: 2135100
D. mel: MB018B/CyO	Karla Kaun	Janelia: 2135069
D. mel: MB027B	Karla Kaun	Janelia: 2135078
D. mel: MB549C/TM6b	Karla Kaun	Janelia: 2501897
D. mel: MB082C	Karla Kaun	Janelia: 2135130
D. mel: MB434B/CyO	Janelia	Janelia: 2501775
D. mel: MB112C	Janelia	Janelia: 2135209
D. mel: MB011B	Janelia	Janelia: 2135062
D. mel: SS52577	Janelia	Janelia: 3028433
D. mel: SS02255/[TM6b]	Janelia	Janelia: 3018121
D. mel: SS52244/[CyO]	Janelia	Janelia: 3028329
D. mel: SS54549	Janelia	Janelia: 3029433
D. mel: SS02239	Janelia	Janelia: 3018105
D. mel: SS50464	Janelia	Janelia: 3028081
D. mel: SS02718	Janelia	Janelia: 3018714
D. mel: SS50420	Janelia	Janelia: 3028108
D. mel: SS47432	Janelia	Janelia: 3027368
D. mel: orco-GAL4,IR8a-GAL4/[CyO]	this study	
D. mel: 43D09AD;VT000986DB	this study	
D. mel: VT026663AD;12D12DB	this study	
D. mel: VT026663AD;VT027955DB	this study	
D. mel: 43D09AD;65C03DB	this study	
D. mel: 65C03AD;45D04DB	this study	
D. mel: 12D12AD;vt027955DB	this study	
D. mel: VT026663AD;65C03DB	this study	
D. mel: 12D12AD;65C03DB	this study	
D. mel: VT041421AD;28H10DB	this study	
D. mel: VT041421AD;33E06DB	this study	
D. mel: VT041421AD;65H10DB	this study	
D. mel: VT029515AD;78G09DB	this study	
D. mel: 13B10AD;VT029515DB	this study	
D. mel: 13B10AD;VT041421DB	this study	
D. mel: 20XUAS-IVSCsChrimson.mVenus}attP40 (II)	BDSC	RRID: BDSC_55135
D. mel: 20x-UAS-IVS-csChrimson-mVenus-attp2 (III)	BDSC	RRID: BDSC_55136
D. mel: UAS-tdTOM (III)	BDSC	RRID: BDSC_36328

D. mel: norpA^36;T(2,3)En^es/([cyo-afgp;TM3-agfp])	Rachel Wilson	
D. mel: +(HCS);+;P{10xUAS-IVS-Syn21-GFP-p10}attP2 (10X UAS- GFP) (Backcrossed)	Michael Dickinson	
D. mel: UAS-GCaMP6f;UAS-tdTOM	Michael Dickinson	
D. mel: w[*]; P{w[+mC] = UAS-TeTxLC.tnt}E2 (UAS-TNTe)	Matthieu Louis	
tsh-Gal80(w-)/CyO (y)	Julie Simpson via Richard Mann	
D. mel: UAS-myrGFP, QUAS-mtdTomato (3x HA); trans-Tango	Gilad Barnea	
D. mel: UAS(FRT.stop)CsChrimson.mVenus/P{hs-hid}Y; LexAop-FLP/(CyO); ChAT-LexA/TM6b	Matthew Clark	
D. mel: UAS(FRT.stop)CsChrimson.mVenus/P{hs-hid}Y; LexAop-FLP; Gad1-LexA/TM3 sb	Matthew Clark	
D. mel: CLIN: dpn(KDRT.stop)cre.PEST ; Act(loxP.GAL80.stop)lexA::p65, lexAop-rCD2::RFP,UAS-mCD8:: GFP-p10; Stg14KD/TM6B, Tb[+]	Mubarak Syed	RRID:BDSC_67094 and RRID:BDSC_67089
D. mel: norpA^{36};UAS-Chrimson/[CyO.a-GFP];10x UAS-GFP	this study	
D. mel: norpA^{36};tsh-Gal80/cyo-agfp;UAS-Chrimson-mVenus	this study	
D.mel: norpA^{36}; s/cyo; UAS-GTACR1-EYFP/TM6b	Claude Desplan	
D. mel: norpA^{36} (backcrossed in w118)	Alvarez-Salvado et al., 2018	
software/algorithms/datsets		
MATLAB		https://www.mathworks.com/products/matlab.html
ImageJ/FIJI		https://imagej.net/Fiji

miniature windtunnels	Alvarez-Salvado et al., 2018	https://doi.org/10.5061/dryad.g27mq71
neuprint hemibrain version 1.2	Scheffer et al., 2020	https://neuprint.janelia.org/?dataset=hemibrain%3Av1.2&qt=findneurons

Data Availability

Data generated during the study will be made available on Dryad on publication. All original code will be made available on Github on publication. Any additional information required to reanalyze the data reported in this paper is available from the Lead Contact upon request.

Materials availability

No new transgenes were created for this study. Transgenic stocks are available on request from the Lead Contact.

Materials and Correspondence: Further information and requests for resources and reagents should be directed to and will be fulfilled by the lead contact, Katherine Nagel (katherine.nagel@nyumc.org).

References

Álvarez-Salvado, E., Licata, A.M., Connor, E.G., McHugh, M.K., King, B.M., Stavropoulos, N., Victor, J.D., Crimaldi, J.P. and Nagel, K.I., 2018. Elementary sensory-motor transformations underlying olfactory navigation in walking fruit-flies. *Elife*, *7*, p.e37815.

Ardin, P., Peng, F., Mangan, M., Lagogiannis, K. and Webb, B., 2016. Using an insect mushroom body circuit to encode route memory in complex natural environments. *PLoS computational biology*, *12*(2), p.e1004683.

Aso, Y., Sitaraman, D., Ichinose, T., Kaun, K.R., Vogt, K., Belliart-Guérin, G., Plaçais, P.Y., Robie, A.A., Yamagata, N., Schnaitmann, C. and Rowell, W.J., 2014. Mushroom body output neurons encode valence and guide memory-based action selection in Drosophila. *Elife*, *3*, p.e04580.

Auer, T.O., Khallaf, M.A., Silbering, A.F., Zappia, G., Ellis, K., Álvarez-Ocaña, R., Arguello, J.R., Hansson, B.S., Jefferis, G.S., Caron, S.J. and Knaden, M., 2020. Olfactory receptor and circuit evolution promote host specialization. *Nature*, *579*(7799), pp.402-408.

Badel, L., Ohta, K., Tsuchimoto, Y. and Kazama, H., 2016. Decoding of context-dependent olfactory behavior in Drosophila. *Neuron*, *91*(1), pp.155-167.

Bates, A.S., Schlegel, P., Roberts, R.J., Drummond, N., Tamimi, I.F., Turnbull, R., Zhao, X., Marin, E.C., Popovici, P.D., Dhawan, S. and Jamasb, A., 2020. Complete connectomic reconstruction of olfactory projection neurons in the fly brain. *Current Biology*, *30*(16), pp.3183-3199.

Bell, W.J. and Kramer, E., 1979. Search and anemotactic orientation of cockroaches. *Journal of Insect Physiology*, *25*(8), pp.631-640.

Bell, J.S. and Wilson, R.I., 2016. Behavior reveals selective summation and max pooling among olfactory processing channels. *Neuron*, *91*(2), pp.425-438.

Buehlmann, C., Hansson, B.S. and Knaden, M., 2012. Path integration controls nest-plume following in desert ants. *Current Biology*, *22*(7), pp.645-649.

Cardé, R.T. and Willis, M.A., 2008. Navigational strategies used by insects to find distant, wind-borne sources of odor. *Journal of chemical ecology*, *34*(7), pp.854-866.

Celani, A., Villermaux, E. and Vergassola, M., 2014. Odor landscapes in turbulent environments. *Physical Review X*, *4*(4), p.041015.

Clyne, J.D. and Miesenböck, G., 2008. Sex-specific control and tuning of the pattern generator for courtship song in Drosophila. *Cell*, *133*(2), pp.354-363.

Cognigni, P., Felsenberg, J. and Waddell, S., 2018. Do the right thing: neural network mechanisms of memory formation, expression and update in Drosophila. *Current opinion in neurobiology*, *49*, pp.51-58.

Crimaldi, J.P. and Koseff, J.R., 2001. High-resolution measurements of the spatial and temporal scalar structure of a turbulent plume. *Experiments in Fluids*, *31*(1), pp.90-102.

Currier, T.A., Matheson, A.M. and Nagel, K.I., 2020. Encoding and control of orientation to airflow by a set of Drosophila fan-shaped body neurons. *Elife*, *9*, p.e61510.

Dacke, M., Bell, A.T., Foster, J.J., Baird, E.J., Strube-Bloss, M.F., Byrne, M.J. and El Jundi, B., 2019. Multimodal cue integration in the dung beetle compass. *Proceedings of the National Academy of Sciences*, *116*(28), pp.14248-14253.

David, C.T., Kennedy, J.S. and Ludlow, A.R., 1983. Finding of a sex pheromone source by gypsy moths released in the field. *Nature*, *303*(5920), pp.804-806.

De Belle, J.S. and Heisenberg, M., 1994. Associative odor learning in Drosophila abolished by chemical ablation of mushroom bodies. *Science*, *263*(5147), pp.692-695.

Dolan, M.J., Frechter, S., Bates, A.S., Dan, C., Huoviala, P., Roberts, R.J., Schlegel, P., Dhawan, S., Tabano, R., Dionne, H. and Christoforou, C., 2019. Neurogenetic dissection of the Drosophila lateral horn reveals major outputs, diverse behavioural functions, and interactions with the mushroom body. *Elife*, *8*, p.e43079.

Donlea, J.M., Pimentel, D. and Miesenböck, G., 2014. Neuronal machinery of sleep homeostasis in Drosophila. *Neuron*, *81*(4), pp.860-872.

Fisher, Y.E., Lu, J., D'Alessandro, I. and Wilson, R.I., 2019. Sensorimotor experience remaps visual input to a heading-direction network. *Nature*, *576*(7785), pp.121-125.

Fuller, S.B., Straw, A.D., Peek, M.Y., Murray, R.M. and Dickinson, M.H., 2014. Flying Drosophila stabilize their vision-based velocity controller by sensing wind with their antennae. *Proceedings of the National Academy of Sciences*, *111*(13), pp.E1182-E1191.

Handler, A., Graham, T.G., Cohn, R., Morantte, I., Siliciano, A.F., Zeng, J., Li, Y. and Ruta, V., 2019. Distinct dopamine receptor pathways underlie the temporal sensitivity of associative learning. *Cell*, *178*(1), pp.60-75.

Hargreaves, E.L., Rao, G., Lee, I. and Knierim, J.J., 2005. Major dissociation between medial and lateral entorhinal input to dorsal hippocampus. *science*, *308*(5729), pp.1792-1794.

Hige, T., Aso, Y., Rubin, G.M. and Turner, G.C., 2015. Plasticity-driven individualization of olfactory coding in mushroom body output neurons. *Nature*, *526*(7572), pp.258-262.

Hige, T., Aso, Y., Modi, M.N., Rubin, G.M. and Turner, G.C., 2015. Heterosynaptic plasticity underlies aversive olfactory learning in Drosophila. *Neuron*, *88*(5), pp.985-998.

Honkanen, A., Adden, A., da Silva Freitas, J. and Heinze, S., 2019. The insect central complex and the neural basis of navigational strategies. *Journal of Experimental Biology*, *222*(Suppl_1), p.jeb188854.

Homberg, U., 1985. Interneurones of the central complex in the bee brain (Apis mellifera, L.). *Journal of insect physiology*, *31*(3), pp.251-264.

Hulse, B.K., Haberkern, H., Franconville, R., Turner-Evans, D.B., Takemura, S., Wolff, T., Noorman, M., Dreher, M., Dan, C., Parekh, R. and Hermundstad, A.M., 2021. A connectome of the Drosophila central complex reveals network motifs suitable for flexible navigation and context-dependent action selection. *Elife,* 10:e66039.

Jung, S.H., Hueston, C. and Bhandawat, V., 2015. Odor-identity dependent motor programs underlie behavioral responses to odors. *Elife*, *4*, p.e11092.

Kahsai, L. and Winther, Å.M., 2011. Chemical neuroanatomy of the Drosophila central complex: distribution of multiple neuropeptides in relation to neurotransmitters. *Journal of Comparative Neurology*, *519*(2), pp.290-315.

Kennedy, J.S. and Marsh, D., 1974. Pheromone-regulated anemotaxis in flying moths. *Science*, *184*(4140), pp.999-1001.

Kobler, J.M., Jimenez, F.J.R., Petcu, I. and Kadow, I.C.G., 2020. Immune receptor signaling and the mushroom body mediate post-ingestion pathogen avoidance. *Current Biology*, *30*(23), pp.4693-4709.

Larsson, M.C., Domingos, A.I., Jones, W.D., Chiappe, M.E., Amrein, H. and Vosshall, L.B., 2004. Or83b encodes a broadly expressed odorant receptor essential for Drosophila olfaction. *Neuron*, *43*(5), pp.703-714.

Leitner, F.C., Melzer, S., Lütcke, H., Pinna, R., Seeburg, P.H., Helmchen, F. and Monyer, H., 2016. Spatially segregated feedforward and feedback neurons support differential odor processing in the lateral entorhinal cortex. *Nature neuroscience*, *19*(7), pp.935-944.

Le Moël, F., Stone, T., Lihoreau, M., Wystrach, A. and Webb, B., 2019. The central complex as a potential substrate for vector based navigation. *Frontiers in psychology*, *10*, p.690.

Li, F., Lindsey, J.W., Marin, E.C., Otto, N., Dreher, M., Dempsey, G., Stark, I., Bates, A.S., Pleijzier, M.W., Schlegel, P. and Nern, A., 2020. The connectome of the adult Drosophila mushroom body provides insights into function. *Elife*, *9*, p.e62576.

Lu, J., Westeinde, E.A., Hamburg, L., Dawson, P.M., Lyu, C., Maimon, G., Druckmann, S. and Wilson, R.I., 2020. Transforming representations of movement from body-to world-centric space. *bioRxiv*.

Lyu, C., Abbott, L.F. and Maimon, G., 2020. A neuronal circuit for vector computation builds an allocentric traveling-direction signal in the Drosophila fan-shaped body. *bioRxiv*.

Mamiya, A., Beshel, J., Xu, C. and Zhong, Y., 2008. Neural representations of airflow in Drosophila mushroom body. *PLoS One*, *3*(12), p.e4063.

Martin, J.P., Guo, P., Mu, L., Harley, C.M. and Ritzmann, R.E., 2015. Central-complex control of movement in the freely walking cockroach. *Current Biology*, *25*(21), pp.2795-2803.

Mishkin, M., Ungerleider, L.G. and Macko, K.A., 1983. Object vision and spatial vision: two cortical pathways. *Trends in neurosciences*, *6*, pp.414-417.

Murlis, J., Elkinton, J.S. and Carde, R.T., 1992. Odor plumes and how insects use them. *Annual review of entomology*, *37*(1), pp.505-532.

Namiki, S. and Kanzaki, R., 2016. Comparative neuroanatomy of the lateral accessory lobe in the insect brain. *Frontiers in Physiology*, *7*, p.244.

Okubo, T.S., Patella, P., D'Alessandro, I. and Wilson, R.I., 2020. A neural network for wind-guided compass navigation. *Neuron*, *107*(5), pp.924-940.

Omoto, J.J., Keleş, M.F., Nguyen, B.C.M., Bolanos, C., Lovick, J.K., Frye, M.A. and Hartenstein, V., 2017. Visual input to the Drosophila central complex by developmentally and functionally distinct neuronal populations. *Current Biology*, *27*(8), pp.1098-1110.

Owald, D., Felsenberg, J., Talbot, C.B., Das, G., Perisse, E., Huetteroth, W. and Waddell, S., 2015. Activity of defined mushroom body output neurons underlies learned olfactory behavior in Drosophila. *Neuron*, *86*(2), pp.417-427.

Page, J.L., Dickman, B.D., Webster, D.R. and Weissburg, M.J., 2011. Getting ahead: context-dependent responses to odorant filaments drive along-stream progress during odor tracking in blue crabs. *Journal of Experimental Biology*, *214*(9), pp.1498-1512.

Rayshubskiy, A., Holtz, S.L. , D'Alessandro, I. , Li, A.A., Vanderbeck, Q.X., Haber, I.S., Gibb, P.W., and Wilson, R.I 2020. Neural circuit mechanisms for steering control in walking *Drosophila* bioRxiv 2020.04.04.024703;

Ren, Q., Awasaki, T., Huang, Y.F., Liu, Z. and Lee, T., 2016. Cell class-lineage analysis reveals sexually dimorphic lineage compositions in the Drosophila brain. *Current Biology*, *26*(19), pp.2583-2593.

Sareen, P.F., McCurdy, L.Y. and Nitabach, M.N., 2021. A neuronal ensemble encoding adaptive choice during sensory conflict in Drosophila. *Nature communications*, *12*(1), pp.1-13.

Sayin, S., De Backer, J.F., Siju, K.P., Wosniack, M.E., Lewis, L.P., Frisch, L.M., Gansen, B., Schlegel, P., Edmondson-Stait, A., Sharifi, N. and Fisher, C.B., 2019. A neural circuit arbitrates between persistence and withdrawal in hungry Drosophila. *Neuron*, *104*(3), pp.544-558.

Scaplen, K.M., Talay, M., Fisher, J.D., Cohn, R., Sorkaç, A., Aso, Y., Barnea, G. and Kaun, K.R., 2021. Transsynaptic mapping of Drosophila mushroom body output neurons. *Elife*, *10*, p.e63379.

Scheffer, L.K., Xu, C.S., Januszewski, M., Lu, Z., Takemura, S.Y., Hayworth, K.J., Huang, G.B., Shinomiya, K., Maitlin-Shepard, J., Berg, S. and Clements, J., 2020. A connectome and analysis of the adult Drosophila central brain. *Elife*, *9*, p.e57443.

Schlegel, P., Bates, A.S., Stürner, T., Jagannathan, S.R., Drummond, N., Hsu, J., Capdevila, L.S., Javier, A., Marin, E.C., Barth-Maron, A. and Tamimi, I.F., 2021. Information flow, cell types and stereotypy in a full olfactory connectome. *Elife*, *10*, p.e66018.

Seelig, J.D. and Jayaraman, V., 2015. Neural dynamics for landmark orientation and angular path integration. *Nature*, *521*(7551), pp.186-191.

Silbering, A.F., Rytz, R., Grosjean, Y., Abuin, L., Ramdya, P., Jefferis, G.S. and Benton, R., 2011. Complementary function and integrated wiring of the evolutionarily distinct Drosophila olfactory subsystems. *Journal of Neuroscience*, *31*(38), pp.13357-13375.

Stone, T., Webb, B., Adden, A., Weddig, N.B., Honkanen, A., Templin, R., Wcislo, W., Scimeca, L., Warrant, E. and Heinze, S., 2017. An anatomically constrained model for path integration in the bee brain. *Current Biology*, *27*(20), pp.3069-3085.

Strauss, R. and Heisenberg, M., 1993. A higher control center of locomotor behavior in the Drosophila brain. *Journal of Neuroscience*, *13*(5), pp.1852-1861.

Sun, X., Yue, S. and Mangan, M., 2020. A decentralised neural model explaining optimal integration of navigational strategies in insects. *Elife*, *9*, p.e54026.

Sun, X., Yue, S. and Mangan, M., 2021. How the insect central complex could coordinate multimodal navigation. *bioRxiv*.

Suver, M.P., Matheson, A.M., Sarkar, S., Damiata, M., Schoppik, D. and Nagel, K.I., 2019. Encoding of wind direction by central neurons in Drosophila. *Neuron*, *102*(4), pp.828-842.

Talay, M., Richman, E.B., Snell, N.J., Hartmann, G.G., Fisher, J.D., Sorkaç, A., Santoyo, J.F., Chou-Freed, C., Nair, N., Johnson, M. and Szymanski, J.R., 2017. Transsynaptic mapping of second-order taste neurons in flies by trans-Tango. *Neuron*, *96*(4), pp.783-795.

van Breugel, F. and Dickinson, M.H., 2014. Plume-tracking behavior of flying Drosophila emerges from a set of distinct sensory-motor reflexes. *Current Biology*, *24*(3), pp.274-286.

Webster, D.R. and Weissburg, M.J., 2001. Chemosensory guidance cues in a turbulent chemical odor plume. *Limnology and Oceanography*, *46*(5), pp.1034-1047.

Wolf, H. and Wehner, R., 2000. Pinpointing food sources: olfactory and anemotactic orientation in desert ants, Cataglyphis fortis. *Journal of Experimental Biology*, *203*(5), pp.857-868.

Methods References:

Giovannucci A, Friedrich J, Gunn P, Kalfon J, Brown BL, Koay SA, Taxidis J, Najafi F, Gauthier JL, Zhou P, Khakh BS, Tank DW, Chklovskii DB, Pnevmatikakis EA. 2019. CaImAn an

open source tool for scalable calcium imaging data analysis. eLife 8:e38173. DOI: https://doi.org/10.7554/eLife.38173, PMID: 30652683

Muir DR, Kampa BM. 2014. FocusStack and StimServer: a new open source MATLAB toolchain for visual stimulation and analysis of two-photon calcium neuronal imaging data. Frontiers in Neuroinformatics 8:85. DOI: https://doi.org/10.3389/fninf.2014.00085, PMID: 25653614

Nagel KI, Wilson RI. 2016. Mechanisms underlying population response dynamics in inhibitory interneurons of the Drosophila Antennal Lobe. The Journal of Neuroscience 36:4325–4338. DOI: https://doi.org/10.1523/JNEUROSCI.3887-15.2016, PMID: 27076428

Pnevmatikakis EA, Giovannucci A. 2017. NoRMCorre: an online algorithm for piecewise rigid motion correction of calcium imaging data. Journal of Neuroscience Methods 291:83–94. DOI: https://doi.org/10.1016/j.jneumeth.2017.07.031, PMID: 28782629

Figure 1

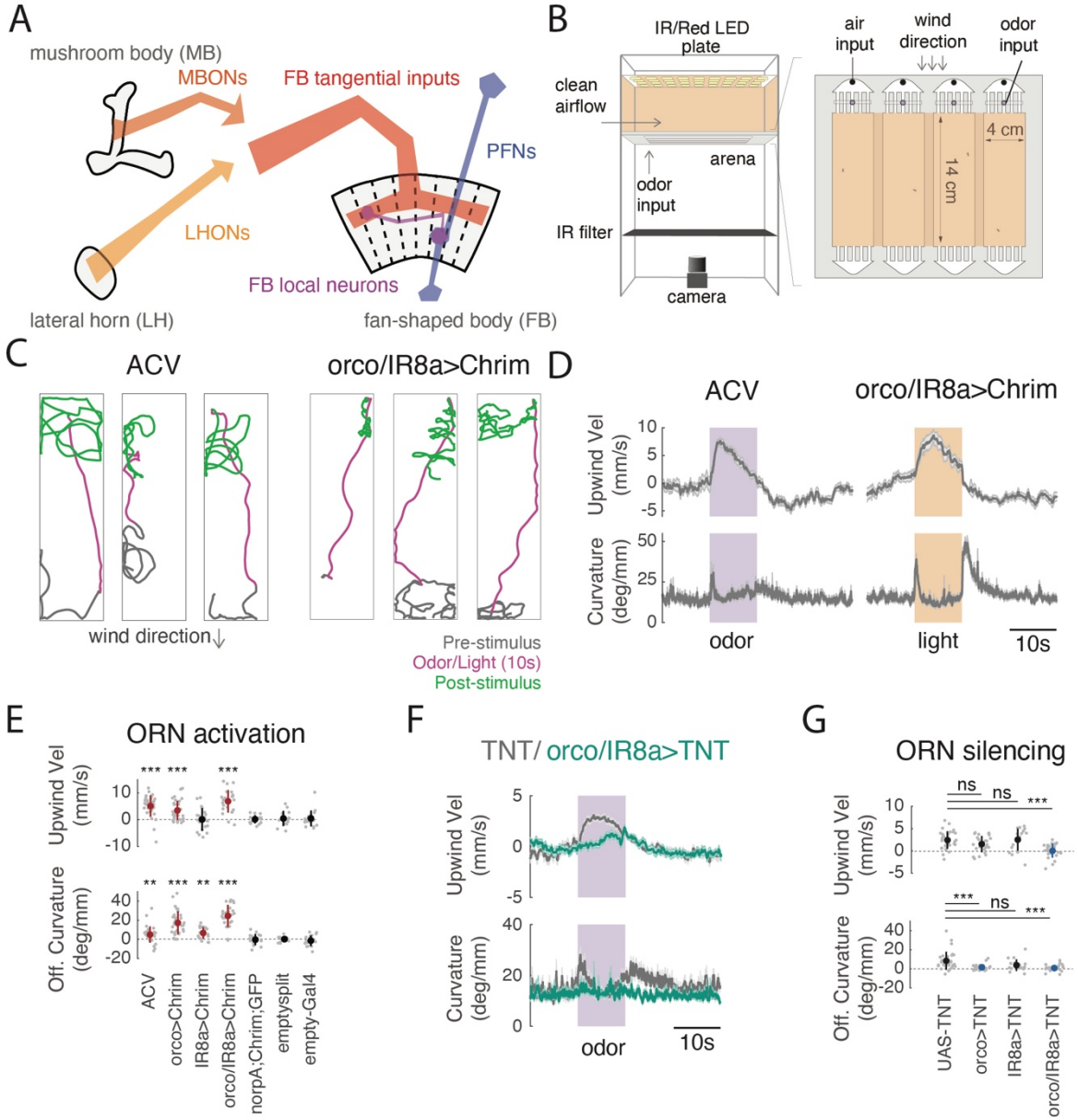

Fig. 1: A behavioral paradigm for investigating odor-evoked wind navigation

A) Diagram of brain regions and neuronal classes investigated in this study. The mushroom body (MB) is required for olfactory learning while the lateral horn (LH) is thought to perform innate olfactory processing. The fan-shaped body (FB) is part of the central complex, and is thought to play a role in spatially-oriented navigation. Output neurons of the MB and LH (MBONs and LHONs) provide input directly or indirectly to FB tangential inputs (Li et al. 2020, Scheffer et al. 2020, Hulse et al. 2021). The FB also receives input from columnar cells (PFNs) that have been shown to strongly encode wind direction information (Currier et al. 2020). FB

local neurons receive input both from FB tangential inputs and from columnar PFNs (Hulse et al. 2021).

B) Schematic of top and side view of the behavioral apparatus showing IR illumination (850nm), red activation light (626nm, 26μW/mm^2), imaging camera, behavioral chambers, and air and odor inputs.

C) Navigation behaviors evoked by odor and optogenetic stimulation of olfactory receptor neurons. Example walking trajectories in response to apple cider vinegar (left, ACV, 1%) and optogenetic activation of orco+ and IR8a+ ORNs (right), before (gray), during (magenta), and after (green) 10s of odor (left) or light (right). Wind was constant at 11.9 cm/s.

D) Time course of upwind velocity and curvature (angular/forward velocity) in response to odor or optogenetic stimulation, averaged across flies (mean±SEM, ACV N= 26 flies, ORN activation N= 24 flies). shaded area: stimulation period (10s 1%ACV (purple) or 10s light (orange) respectively).

E) Upwind velocity and offset curvature (average change from baseline for single flies) in response to stimulation for each genotype/condition. Mean±STD overlaid; red indicates a significant increase. ACV, orco>Chrimson, and orco/IR8a>Chrimson stimulation all drove significant increases in upwind velocity (0-5 s after stimulus onset, Wilcoxon signed rank test: ACV: p= 1.0997e-05, orco: p=3.8672e-05, orco,ir8a: 2.6691e-05) and offset curvature (0-2 s after stimulus offset, Wilcoxon signed rank test ACV: p=1.9619e-04, orco: p=1.1742e-06, orco,ir8a: p=2.3518e-05). Light activation of flies carrying only the parental effector (norpA;UAS-Chrimson), empty-GAL4>Chrimson, or empty-split GAL4>Chrimson did not increase upwind velocity (Wilcoxon signed rank test: parent: p= 0.7174, empty-split: p=0.6874, empty-gal4: p=0.6698) or offset curvature (Wilcoxon signed rank test: parent: p= 0.7960, empty-split: p=0.3144 ,empty gal4: p=0.7354). IR8a>Chrimson stimulation did not increase upwind velocity (p=0.3507) but did increase offset curvature (p=4.4934e-04).

F) Time course of upwind velocity and curvature in response to odor in flies with all ACV-sensitive ORNs silenced (orco/IR8a>TNT, mean±SEM, N=26, teal) versus control (UAS-TNT, N= 31, gray).

G) Upwind velocity and offset curvature for silencing experiments, quantified as in **E**. Blue overlay represents significant decrease compared to control (UAS-TNT). (Mann-Whitney U test compared to UAS-TNT control, upwind velocity: orco: p= 0.10627, ir8a: p=0.40095, orco,ir8a: p=0.00010917, offset curvature: orco: p=3.2758e-05, ir8a: p=0.037135, orco,ir8a: p=4.2482e-05)

All comparisons were corrected using the Bonferroni method (see Methods).

Supplementary Figure 1

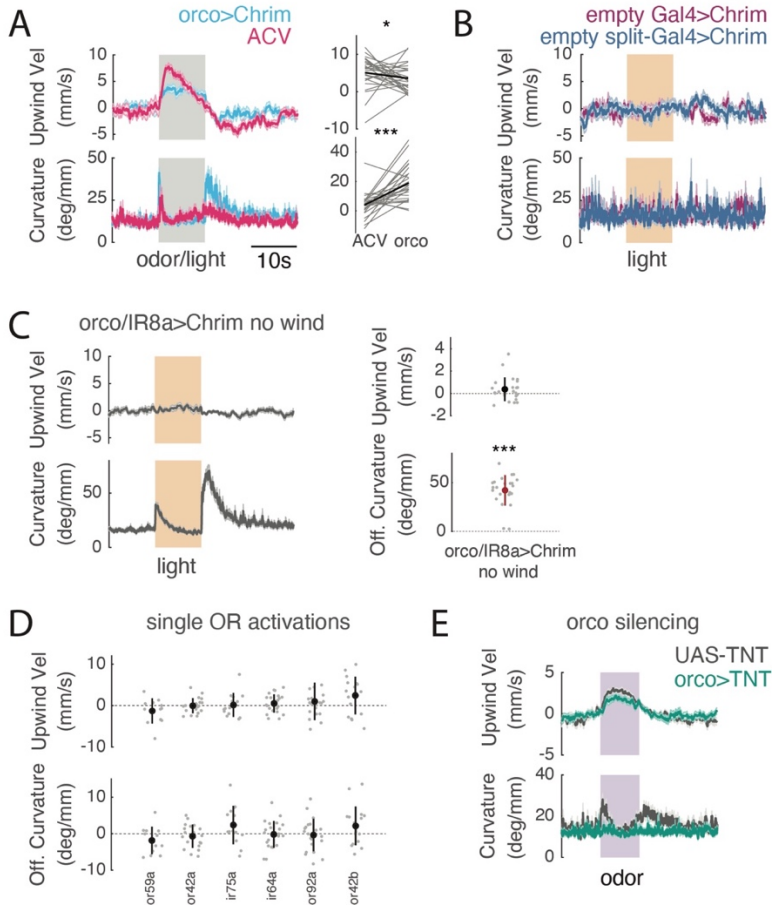

Fig. S1: Additional data on ORN encoding of olfactory navigation behavior

A) Left: Upwind velocity and curvature time courses (mean±SEM) in the same flies (N = 26 flies) exposed to both 1% ACV (pink) and optogenetic stimulation of orco+ ORNs (blue) in interleaved trials. Right: Comparison of average upwind velocity (0-5s after stimulus onset) and offset curvature (0-2s after stimulus offset) for each fly. Within each fly, ACV evoked greater upwind velocity than orco stimulation (Wilcoxon signed rank test: p=0.0319) but weaker offset curvature than orco stimulation (Wilcoxon sign rank test: p=1.3216e-04).

B) Upwind velocity and curvature time courses (mean±SEM) for control flies: empty-GAL4>Chrimson (purple, N= 19) and empty split-GAL4>Chrimson (blue, N= 14). No significant change in either parameter during stimulation (quantified in Figure 1D).

C) Right: Upwind velocity and curvature time courses (mean±SEM) for orco/IR8a>Chrimson flies in the absence of wind (N= 24 flies, see also Alvarez-Salvado et al., 2018 and Suver et al., 2019). Left: quantification as in Fig. 1D. No increase in upwind velocity (Wilcoxon signed rank test, p= 0.0191), but offset curvature increases significantly increases after stimulation (Wilcoxon signed rank test, p= 1.8215e-05).

D) Upwind velocity and offset curvature (average change from baseline for single flies, mean ±STD overlaid) for each single ORN that responds to ACV (Jung et al., 2015). No significant

increase in upwind velocity (Wilcoxon sign rank test, p= 0.2334, 0.7089, 0.9032, 0.3304, 0.3754, 0.0442) or offset curvature (Wilcoxon sign rank test, p= 0.1763, 0.3317, 0.0785, 0.7151, 0.6639, 0.1488).

E) Timecourse of upwind velocity and curvature for flies with orco+ ORNs silenced using orco>TNT (N= 25 flies, teal) versus UAS-TNT controls (N= 31 flies, gray).

All comparisons for behavioral experiments Bonferroni corrected for multiple comparisons.

Figure 2

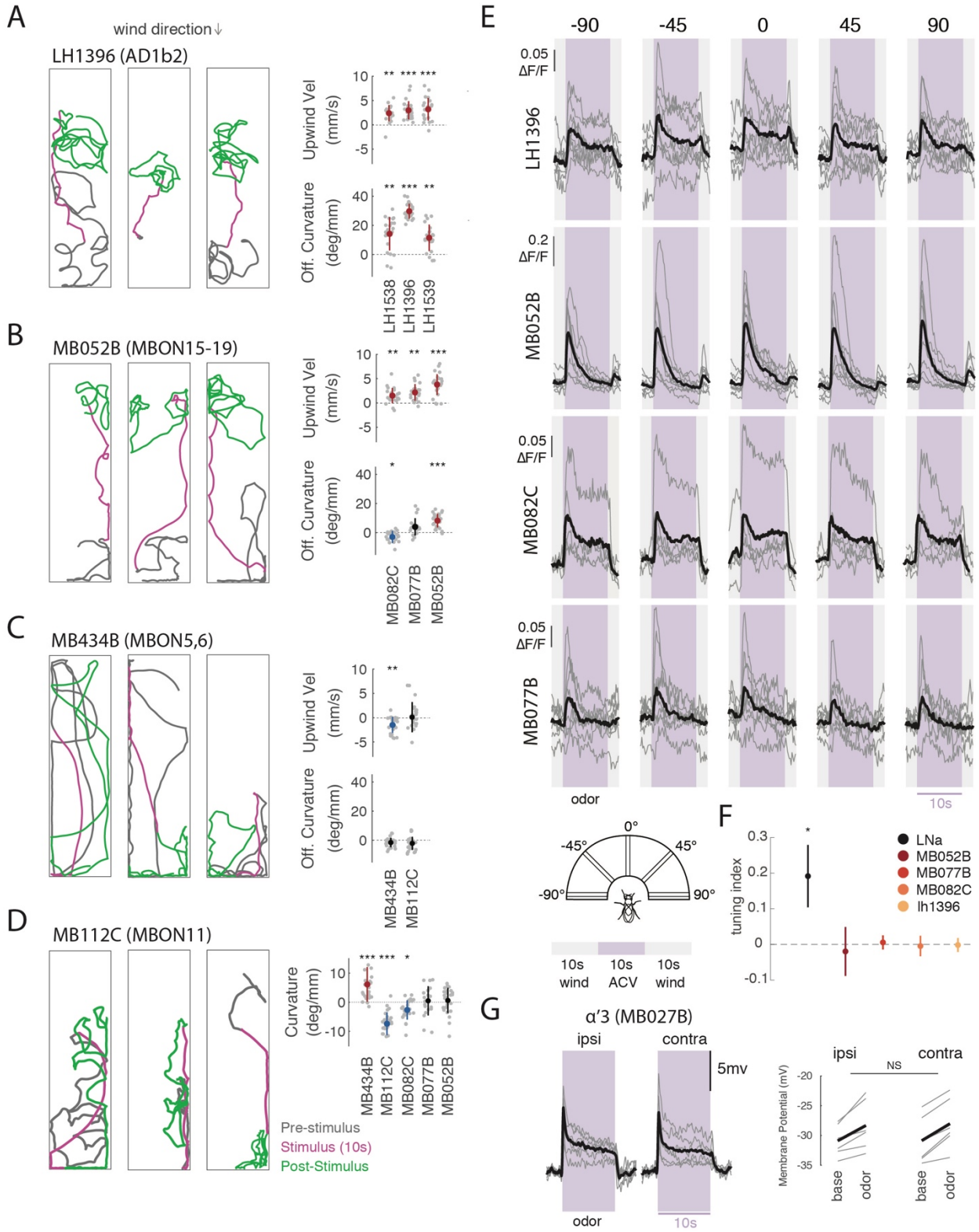
A
wind direction
LH1396 (AD1b2)
Upwind Vel (mm/s)
Off. Curvature (deg/mm)
LH1538
LH1396
LH1539
B
MB052B (MBON15-19)
MB082C
MB077B
MB052B
C
MB434B (MBON5,6)
MB434B
MB112C
D
MB112C (MBON11)
Curvature (deg/mm)
Pre-stimulus
Stimulus (10s)
Post-Stimulus
E
-90
-45
0
45
90
0.05 ΔF/F
0.2 ΔF/F
LH1396
MB052B
MB082C
MB077B
odor
10s
0°
-45°
45°
-90°
90°
10s wind
10s ACV
10s wind
F
tuning index
LNa
MB052B
MB077B
MB082C
lh1396
G
α'3 (MB027B)
ipsi
contra
5mv
odor
10s
Membrane Potential (mV)
NS
base
odor

Fig. 2: LH and MB output neurons promote wind navigation behavior but encode odor independent of wind direction

A) Optogenetic activation of AD1b2 LHONs drives upwind movement and offset search. Left: Example behavioral trajectories in response to optogenetic activation of AD1b2 LHONs labelled by the line LH1396 (left). Right: Upwind velocity and offset curvature (quantified as in Fig. 1D) for three lines that label AD1b2 LHONs (LH1538, LH1539, LH1396). All three lines significantly increase both upwind velocity and offset curvature (Wilcoxon signed rank test, upwind: p= 2.4548e-04, 7.9941e-05, 1.8215e-05; offset-curvature: p= 3.6712e-04, 1.7699e-04, 1.8215e-05 respectively)

B) Optogenetic activation of attraction-promoting MBONs drives upwind movement and offset search. Left: Example behavioral trajectories in response to optogenetic activation of MBONs15-19 labelled by the line MB052B (left). Right: Upwind velocity and offset curvature quantification for three cholinergic MB lines: MB052B, MB077B, and MB082C. Each line labels distinct MBONs. All increase upwind velocity (Wilcoxon signed rank test, p= 1.0997e-05, 1.2267e-04, 2.0378e-04) while MB052B increases offset curvature (p= 6.2811e-06), MB077B does not (p= 0.0046) and MB082C reduced offset curvature (p= 0.0018).

C) Activation of aversion-promoting MBONs promotes downwind movement. Left: Example behavioral trajectories in response to optogenetic activation of glutamatergic MBONs 5 and 6, labeled by the line MB434B (left). Right: Upwind velocity and offset curvature for MB434B and MB112C. MB434B significantly decreases upwind velocity (Wilcoxon signed rank test p= 2.2806e-04) while MB112C does not affect upwind velocity (Wilcoxon signed rank test, p= 0.8036). Neither affects offset curvature (p= 0.0258, 0.0179).

D) MBONs promoting straighter trajectories. Example behavioral trajectories in response to optogenetic activation of the GABAergic MBON11, labeled by the line MB112C (left). Right: Curvature during stimulus (from 2-5s after stimulus onset) for MB112C, MB434B, MB052B, and MB077B. MB112C significantly reduces curvature during the stimulus (Wilcoxon signed rank test, p= 3.5150e-06) while MB434B increases curvature (p= 4.3941e-05) and other MB genotypes have no effect (p= 0.4979, 0.2297).

E) Upwind-promoting LHONs and MBONs encode odor independent of wind direction. Calcium responses (ΔF/F) measured in four lines that all drove upwind movement. Responses were measured in LH dendritic processes of LH1396 (N = 8 flies), in output processes of MB052B (N = 9 flies), MB082C (N=5), MB077B (N=8). All responses measured using GCaMP6f in response to odor (10% ACV, purple) and wind (gray) delivered from 5 directions (schematic). Gray traces represent individual flies, black traces represent mean across flies. No significant differences in response as a function of direction were observed for either LH1396, MB052B, MB082C or MB077B (ANOVA: F(4,35)=0.35, p=0.8408, F(4,40)=0.3, p=0.8794, F(4,25)=0.2, p=0.9989, F(4,35)=0.67, p=0.6166).

F) Tuning for wind direction (dynamic range in response to odor delivered from +90 vs -90°) in imaged MB/LH lines versus LNa, which provides wind-direction tuned input to PFNs. Errorbars represent standard deviation of the mean. Tuning index differs from 0 for LNa (student t-test, 0.0081) while MB/LH lines do not. MB052B (p=0.4162), MB077B (p=0.4486), MB082C (p=0.7394), lh1396 (p=0.8125).

G) Membrane potential responses in α'3 MBONs (labeled by MB027B) to 10% ACV presented from 90° ipsilateral or contralateral to the recorded neuron. Black trace represents mean across flies while gray traces represent individual flies (N=6 cells per hemisphere, each from 1 fly). Odor significantly increases membrane voltage both ipsilaterally and contralaterally (paired student t-test p= 0.0018, 0.0159) and is not different between sides (unpaired student t-test p=0.7561).
All comparisons for behavioral data, and tuning index were corrected using the Bonferroni method (see Methods).

Supplementary Figure 2

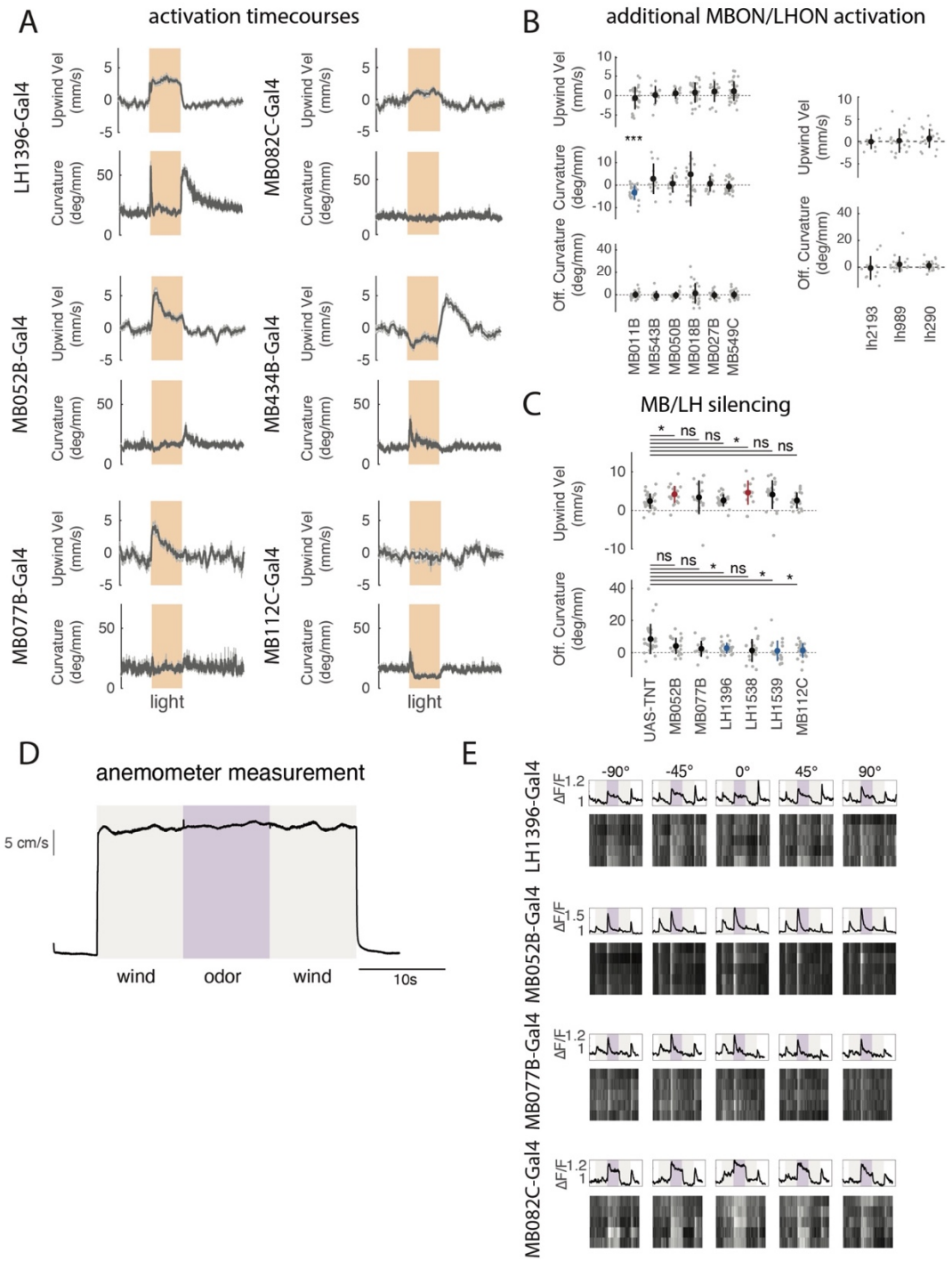

Fig. S2: Additional data on LH and MB responses and behavior

A) Upwind velocity and curvature time courses (mean±SEM) for LH1396>Chrimson (N =24 flies), MB052B>Chrimson (N =27), MB077B>Chrimson (N=21), MB082C>Chrimson (N=24), MB0434B>Chrimson (N =24), and MB112C>Chrimson (N =29).

B) Upwind velocity, curvature during stimulus, and offset curvature for individual MBONs labeled by MB052B (left) and for additional LHONs (right), mean±STD overlaid. MBONs: upwind: MB011B: p=0.3275, MB543B: p=0.5693, MB050B: p=0.1726, MB018B: p=0.1363, MB027B: p=0.1477, MB549C: p=0.0360, curvature: MB0110B: p=3.4071e-05, MB110C: p=0.0027, MB543B: p=0.3804, MB083C: p=3.9023e-04, MB050B: p=0.5016, MB018B: p=0.2029, MB027B: p=0.5695, MB549C: p=0.0742 offset curvature: MB011B: p=0.8376, MB543B: p=0.2061, MB050B: p=0.3910, MB018B: p=0.7533, MB027B: p=0.4380, MB549C: p=0.7807. LHONs: upwind: LH2193: p=0.9658, LH989: p=0.9095, LH290: p=0.0975, offset curvature: LH2193: p=0.7002, LH989: p=0.1997, LH290: p=0.1443.
C) Upwind velocity and offset curvature (quantified as in Fig. 1D) when LHONs and MBONs are silenced. (Mann Whitney U test compared to UAS-TNT control, upwind velocity: MB052B: p=0.0036862, MB077B: p=0.17444, LH1396: p=0.6529, LH1538: p=0.0036449, LH1539: p=0.0090304, MB112C: p=0.83555) offset curvature: MB052B: p=0.063702, MB077B: p=0.012398, LH1396: p=0.0027408, LH1538: p=0.013958, LH1539: p=0.00070953, MB112C: p=0.0011212)
D) Average stimulus delivered to the fly from 3 trials from each of the 5 directions as measured by a hotwire anemometer (average across directions). There is no change in windspeed between wind alone and wind + odor.
E) Single fly examples of calcium responses to wind and odor in LH1396, MB052B, MB077B, and MB082C. Top boxes show average traces for single flies across 5 trials from each direction. Heat maps below depict responses for individual trials.

Figure 3

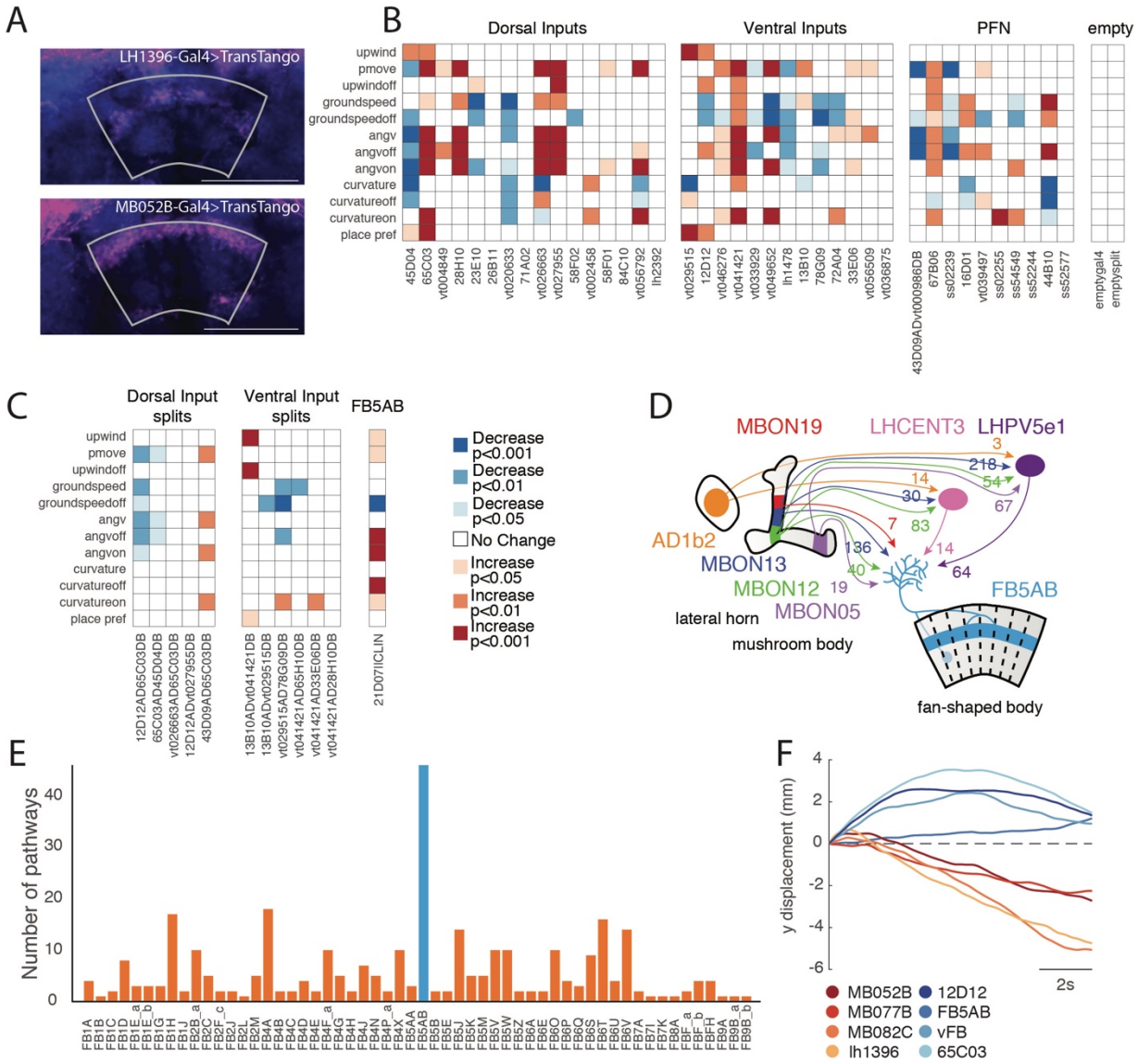

Fig. 3: A set of FB tangential inputs promote wind navigation behavior

A) Trans-synaptic tracing reveals connections between upwind-promoting MB/LH neurons and FB tangential neurons. *Trans-tango* signal driven by LH1396-GAL4 (top) and MB052B-GAL4 (bottom). Trans-synaptic signal (magenta) was observed in horizontal layers of the dorsal FB in both cases. Neuropil is shown in blue. The FB is outlined in gray. Scale bar 50uM.

B) Optogenetic activation results for FB inputs, including dorsal tangential inputs, ventral tangential inputs, columnar PFNs, and empty-GAL4 and empty-split-GAL4 controls. Two dorsal inputs and two ventral inputs drove significant increases in upwind velocity. Control lines drove no significant change in any measured behavioral parameter. See Materials and Methods for calculation of behavioral parameters.

C) Optogenetic activation results for split GAL4 lines labeling dorsal and ventral tangential FB inputs, and for a line labeling FB5AB (21D07-GAL4IICLIN). One split-GAL4 line labeling ventral FB tangential inputs drove a significant increase in upwind velocity.
D) Schematic showing feedforward connectivity onto FB5AB from three upwind-promoting MBONs (MBON 19, MBON 12, MBON 13), one upwind-promoting LHON (AD1b2), and one downwind-promoting MBON (MBON05). Pathways converge onto FB5AB directly or indirectly through LHCENT3 and LHPV5e1. Numbers represent the average synaptic weight between each cell type and the right-sided LHCENT3 (id: 487144598), LHPV5e1 (id: 328611004), or right-sided FB5AB (id: 5813047763).
E) Number of parallel lateral horn pathways from ACV-responsive projection neurons (Jung et al., 2015) to each FB tangential input neuron. Pathways consist of two synapses: the first between the projection neuron and lateral horn neuron, and the second between the lateral horn neuron and the FB tangential input neuron. Blue bar represents the number of pathways converging onto FB5AB.
F) Upwind displacement responses to optogenetic activation of FB tangential input lines outlast the stimulus while responses to activation of MB/LH lines do not. Timecourses of average relative y-displacement (arena position) across flies, following stimulus offset for each line. Individual fly's average positions across trials were set to 0 and relative change in position for 10s following stimulus offset was averaged across flies for each genotype.

Supplementary Figure 3

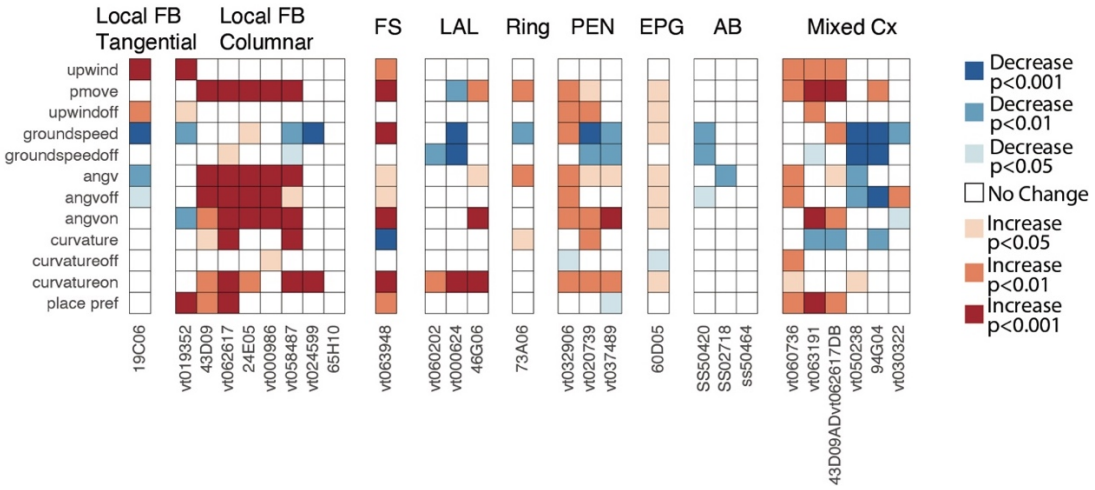

Fig. S3: Additional data from optogenetic screen of Cx neurons

Optogenetic activation data for additional central complex neuron types (Local FB tangential neurons, Local FB columnar neurons, FS neurons, LAL innervating neurons, Ring neurons, PEN neurons, EPG neurons, AB neurons, and drivers that labelled more than one Cx type prominently (mixed)). One local tangential FB neuron line (19C06-GAL4), one local columnar FB neuron line (VT019352-GAL4), and three mixed Cx lines (VT060736-GAL4, VT063191-GAL4, the split line 43D09-AD; VT062617-DB) and one FS neuron line (VT063948-GAL4) produced significant increases in upwind velocity. No LAL, Ring, PEN, or AB lines produced significant changes in upwind velocity, nor did activation of EPG compass neurons (60D05-GAL4). Several FB local columnar neuron lines drove increases in movement probability (Pmove) and angular velocity (angv): 43D09-GAL4, VT062617-GAL4, 24E05-GAL4, VT000986-GAL4, VT058487-GAL4. See Materials and Methods for calculation of behavioral parameters.

Figure 4

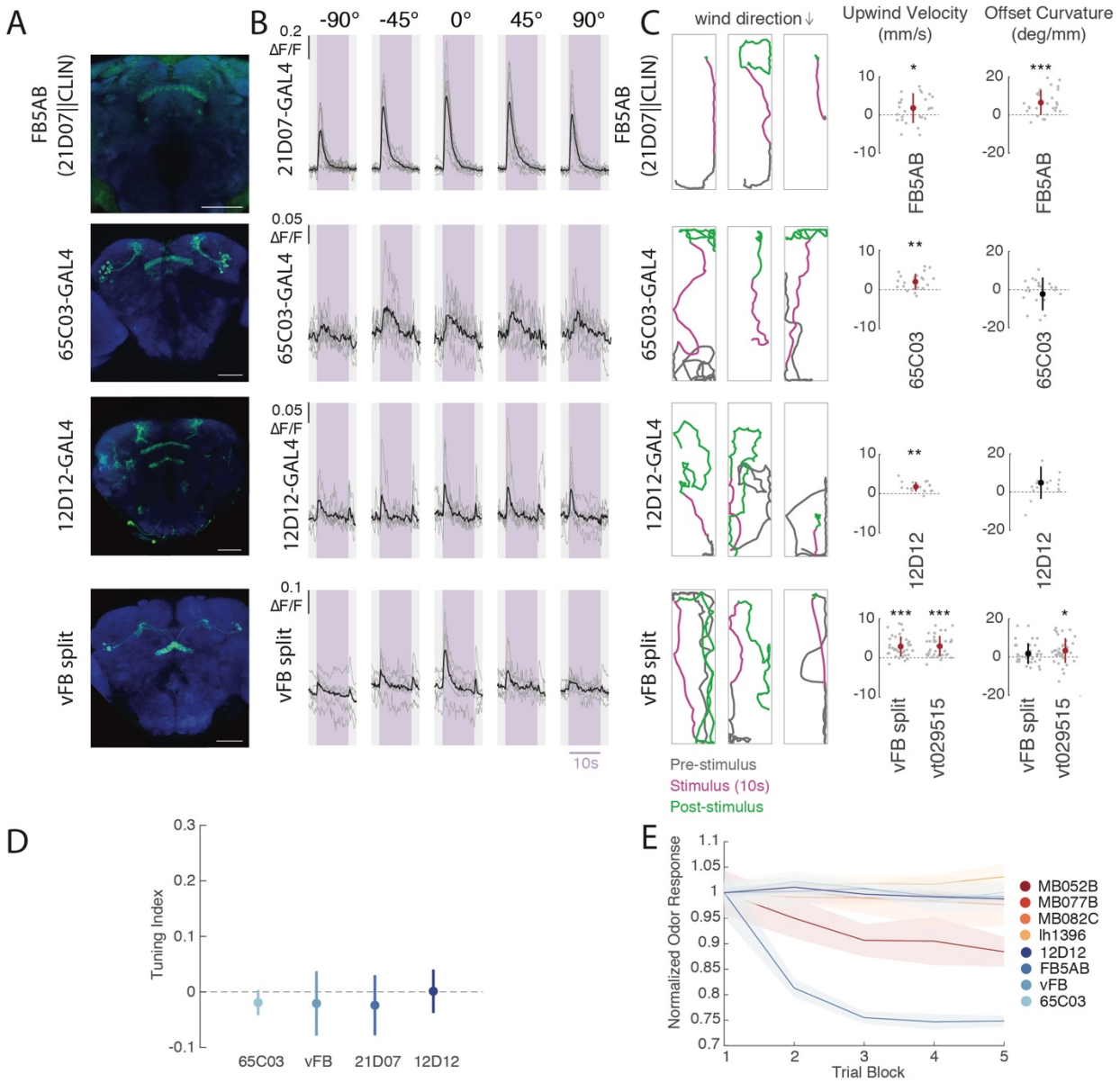

Fig. 4: Multiple FB tangential inputs respond to attractive odor and drive upwind movement

A) Confocal images of lines that showed FB responses to ACV and drove upwind movement when activated. Each image shows stain for mVenus expressed with UAS-Chrimson in flies of the same genotype used for activation experiments (abbreviated genotypes shown at left).

B) Calcium responses in each line shown at left in response to odor delivered from 5 different directions (as in Fig. 2E). Shaded purple region indicates odor period. Gray lines represent individual flies and black represents the mean across flies (21D07-GAL4: N = 9, 65C03-GAL4: N = 7, 12D12-GAL4: N = 6, vFB split: N = 6 flies). No significant difference in response

magnitude was observed between directions (ANOVA: 21D07-GAL4: $F(4,40)=2.14$, $p=0.0938$, 65C03-GAL4: $F(4,30)=0.68$, $p=0.6096$, 12D12-GAL4: $F(4,25)=0.13$, $p=0.971$, vFB split: $F(4,25)=0.64$, $p=0.6358$).

C) Example behavioral trajectories and quantification of upwind velocity and offset curvature in each line shown at left. For FB5AB only light intensity was 34μW/mm^2. For all drivers, upwind velocity was quantified over 0-10s after odor onset. Right: Mean±STD overlaid upwind velocity, offset curvature (Wilcoxon signed rank test: 21D07IICLIN: $p=0.0306$, 8.1448e-05, 65C03-GAL4: $p=4.1850e-04$, 0.5841, 12D12-GAL4: $p=1.8218e-04$, 0.0055 vFB split: $p=3.4153e-07$, 0.1155, VT029515-GAL4 $p=4.3255e-07$, 0.0024).

D) Tuning for wind direction (dynamic range in response to odor delivered from +90 vs -90°) in FB tangential input lines. Error bars represent standard deviation of the mean. Tuning index does not differ from 0 in 65C03 (student t-test: $p=0.0674$), vFB split ($p= 0.4222$), 21D07 ($p=0.2211$), or 12D12 ($p=0.9370$).

E) Decay of fluorescence response to odor over trial blocks. The response to each trial block was calculated as the average odor response to 5 consecutive trials (each from one of the directions), averaged across all flies of a genotype. Response magnitude was normalized by the average response to the first block for each line. Shaded area represents standard error across flies.

All comparisons for behavioral data and tuning index were corrected using the Bonferroni method (see methods)

Supplementary Figure 4

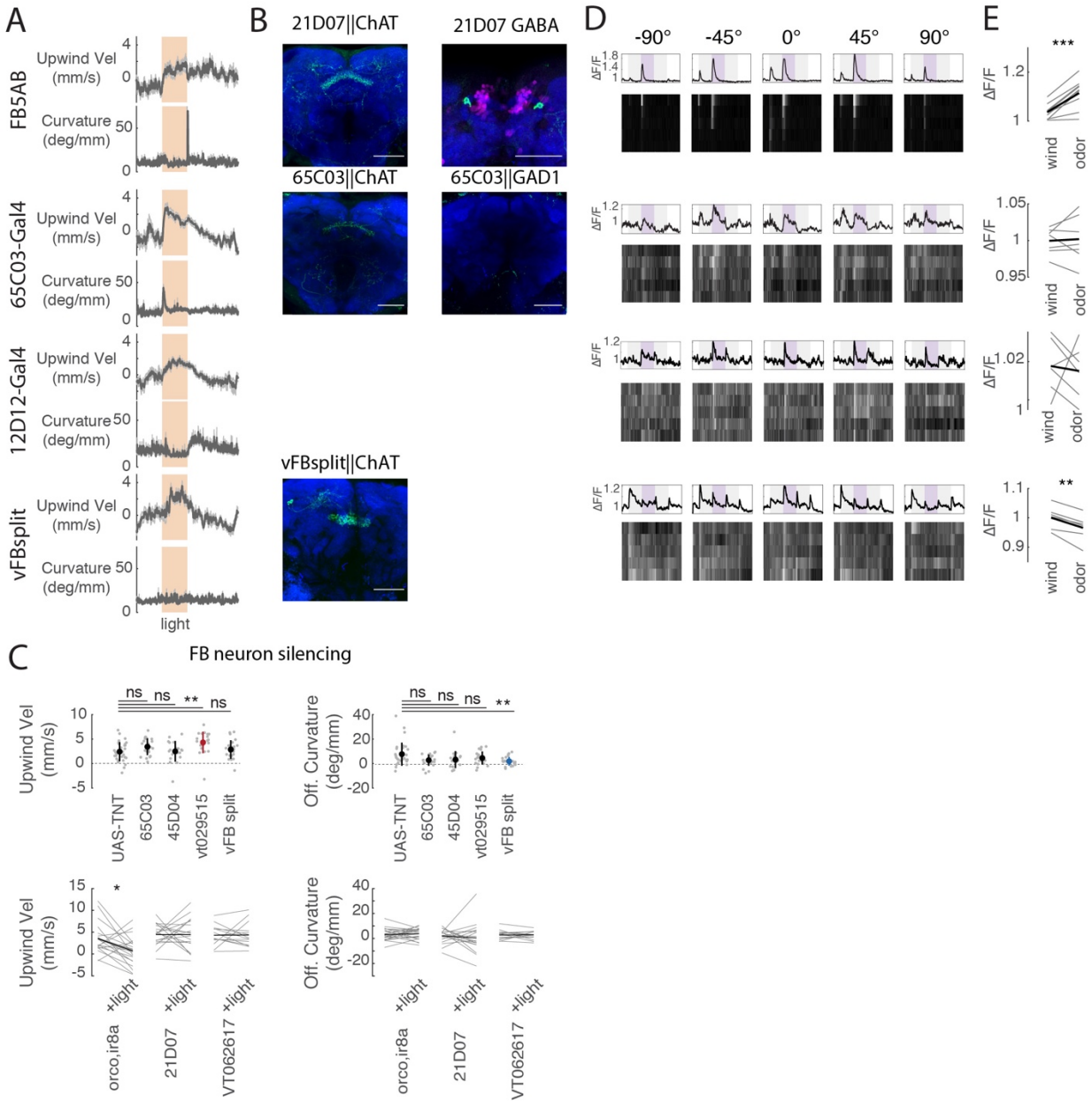

Fig. S4: Additional data on odor-responsive, upwind-promoting FB tangential neurons
A) Timecourses of upwind velocity and curvature averaged across flies for all FB tangential input lines that showed significant responses to ACV (mean±SEM), 21D07IICLIN (N=27), 65C03 (N=24), 12D12 (N=38), vFB split (N=27)).
B) Odor-responsive FB tangential inputs are cholinergic and not GABAergic. Left column: Flies expressing *chrimson-mVenus* under the control of each driver using a ChAT-LexA,LexAOP-FLP strategy (green, see Materials and Methods). Right column: 21D07-GAL4: same genotype as left, but co-stained with anti-GABA (magenta). There is no colocalization of GABA and

Chrimson-mVenus. Flies expressing *Chrimson-mVenus* using a Gad1-LexA, LexAOP-FLP strategy (green) do not label FB neurons in 65C03-GAL4. Scale bars represent 50μM.
C) Top: Effects of silencing FB neurons on behavioral responses to odor (10s 1% ACV). Mean±STD overlaid. (Mann Whitney U test comparing to UAS-TNT control: upwind: 65C03: p=0.048027, 45D04: p=0.65028, vt029515: p=0.00086718, vFB split p=0.60472, offset curvature: 65C03: p=0.044317, 45D04: p=0.087747, vt029515: p=0.31643, vFB split: p=0.0021892). Bottom: Effect of acutely silencing 21D07-GAL4 and VT062617-GAL4 with GTACR1. Orco-GAL4,ir8a-GAL4>GTACR1 silencing is shown as a positive control. Average responses to 10s ACV compared to 10s over ACV overlapped by 10s of light. Individual flies in grey, mean across flies in black. Upwind: orco,ir8a: p=0.0130, 21D07: p=0.9826, vt062617: p=0.5016. Offset curvature: orco,ir8a: p=0.5699, 21D07: p=0.4460, vt062617: p=0.9515. Corrected for multiple comparisons using the Bonferroni method.
D) Example calcium responses from FB tangential inputs in individual flies. Top row depicts average ΔF/F for each direction across 5 trials, heat maps below depict responses in individual trials.
E) Calcium response to wind alone vs ACV. Gray lines represent individual flies and black lines represent genotype means. Significant increase for 21D07-GAL4 (paired student t-test: p=3.9090e-04). No significant increase for 65C03 or 12D12 (paired student's t-test, p=0.7790, p=0.7782) and significant decreases for vFB split (paired student t-test; p = 0.0028)

Figure 5

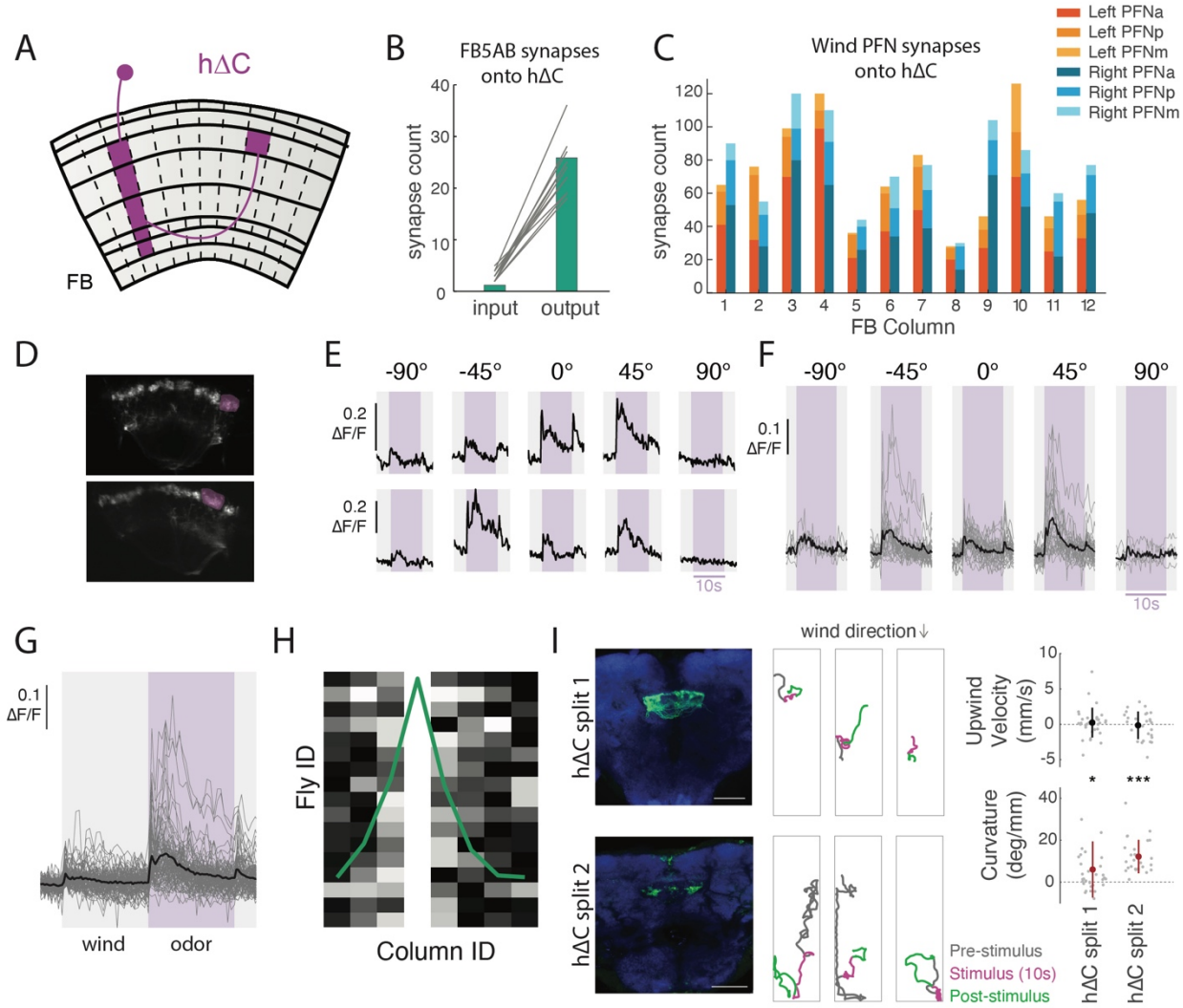

Fig. 5: hΔC neurons integrate odor and wind direction information and drive turning

A) Schematic of an individual hΔC neuron's anatomy (purple). The 20 hΔC neurons that tile the FB each receive input in horizontal layers 2-6 in a single column, and project halfway across the FB, making outputs in horizontal layer 6.

B) Number of FB5AB synapses onto the input and output tufts of hΔC for every FB5AB-hΔC pair.

C) Number of synapses from left and right wind-sensitive PFNs (PFNa, PFNp, and PFNm, tuned to 45° left and right respectively) onto hΔC neurons, summed within columns.

D) 2-photon image of tdTOM expressed with GCaMP6f under VT062617-GAL4 which labels hΔC neurons. Purple ROI drawn around output tuft of a single column for analysis.

E) Odor responses of two example flies/columns showing directionally-tuned odor responses.

F) Summary of all measured odor responses > 2STD above baseline across columns and flies. Gray traces represent individual columns and black traces represent mean across columns.

G) Summary of wind and odor responses for all measured responses > 2STD above baseline across columns and directions. Responses to odor are stronger than those to wind alone (n=87 responsive columns from N=16 Flies).

H) Directional responses are restricted to nearby columns: maximally responsive direction for each fly, where data is phase shifted so maximum columns align at column 4. Each fly normalized to maximum column response.

I) Left: Confocal images of mVenus expressed with UAS-Chrimson driven by two hΔC split GAL4 lines: 19G02AD;VT062617DB (top) and VT026434AD;VT062617DB (bottom). Center: example behavioral trajectories driven by hΔC split-GAL4 activation. Right: Upwind velocity and curvature during stimulus (average change from baseline for single flies), mean±STD overlaid. hΔC activation produces a significant increase in curvature (Wilcoxon signed rank test p = 0.0143, 5.6061e-06) but not upwind velocity (Wilcoxon signed rank test, p=0.3595, 0.8288). Scale bar represents 50μM.

Supplementary Figure 5

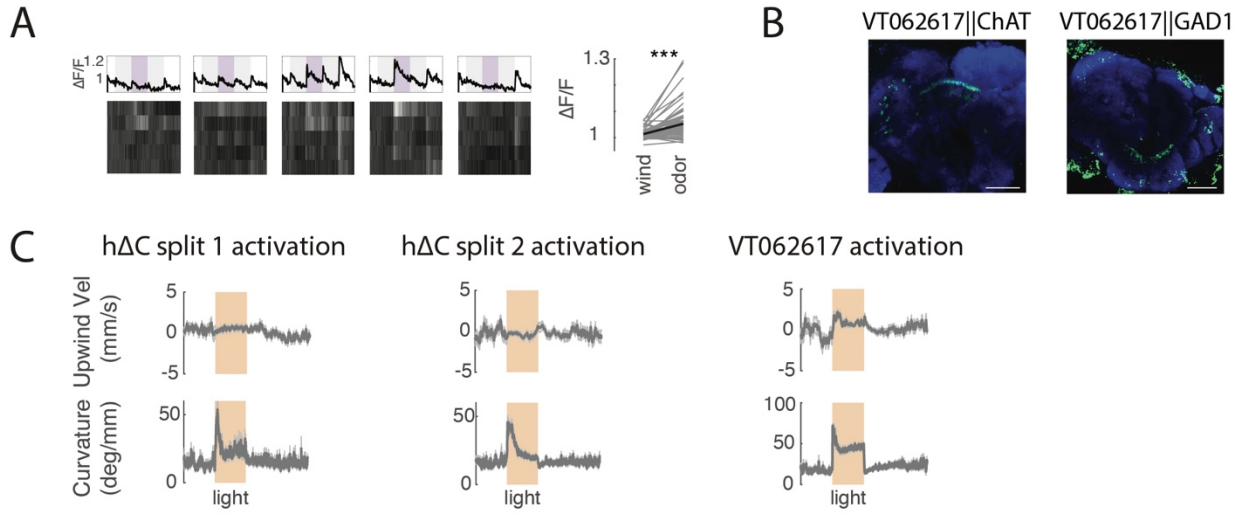

Fig. S5: Additional data on hΔC neurons

A) Calcium response examples from an individual fly for hΔC (left). Top row depicts average ΔF/F for each direction across 5 trials, heat maps below depict responses in individual trials. Right: Calcium response to wind alone (5s after wind onset) vs ACV (5s after odor onset). Gray lines represent average increases of individual active columns. Odor response is significantly larger than wind response (paired student t-test: 4.7885e-11).

B) hΔC neurons are cholinergic. Left column: Flies expressing *chrimson-mVenus* under the control of VT062617-GAL4 using a ChAT-LexA,LexAOP-FLP strategy (green, see Materials and Methods). Right column: Flies expressing *Chrimson-mVenus* using a Gad1-LexA, LexAOP-FLP strategy (green) do not label FB neurons in VT062617-GAL4. Scale bars represent 50μM.

C) Timecourses of upwind velocity and curvature averaged across flies for hΔC split-GAL4s, and for VT062617-GAL4 (N= 32, 27, 23 flies).

Figure 6

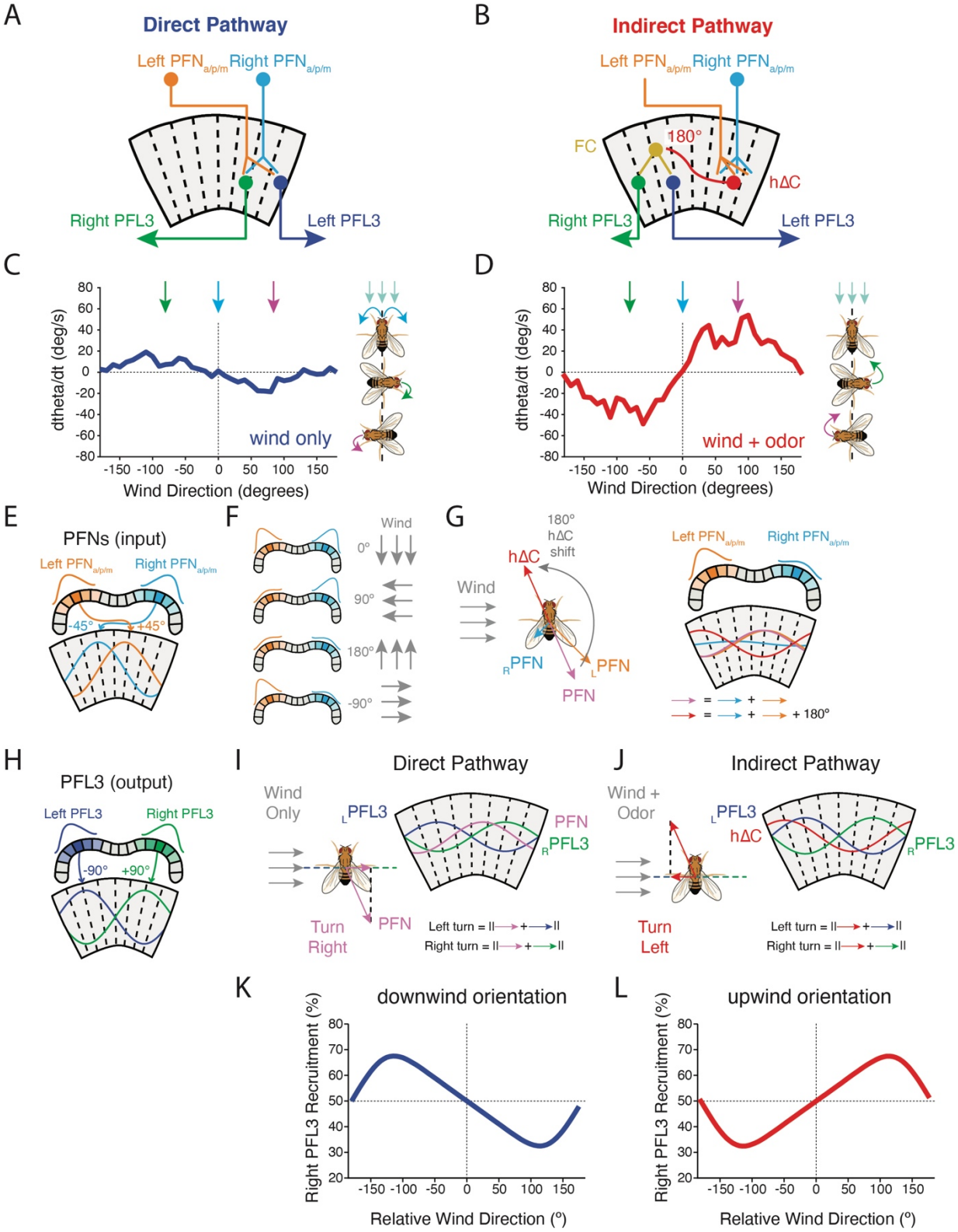
A
Direct Pathway
Left PFN a/p/m
Right PFN a/p/m
Right PFL3
Left PFL3
B
Indirect Pathway
Left PFN a/p/m
Right PFN a/p/m
FC
180°
hΔC
Right PFL3
Left PFL3
C
dtheta/dt (deg/s)
wind only
Wind Direction (degrees)
D
dtheta/dt (deg/s)
wind + odor
Wind Direction (degrees)
E
PFNs (input)
Left PFN a/p/m
Right PFN a/p/m
-45°
+45°
F
Wind
0°
90°
180°
-90°
G
180° hΔC shift
hΔC
Wind
RPFN
LPFN
PFN
Left PFN a/p/m
Right PFN a/p/m
+ 180°
H
PFL3 (output)
Left PFL3
Right PFL3
-90°
+90°
I
Direct Pathway
Wind Only
LPFL3
PFN
RPFL3
Turn Right
PFN
Left turn = II + II
Right turn = II + II
J
Indirect Pathway
Wind + Odor
LPFL3
hΔC
RPFL3
Turn Left
Left turn = II + II
Right turn = II + II
K
downwind orientation
Right PFL3 Recruitment (%)
Relative Wind Direction (°)
L
upwind orientation
Right PFL3 Recruitment (%)
Relative Wind Direction (°)

Fig. 6: A model for olfactory control of wind orientation in the FB

A) Direct pathway from wind-sensitive PFNs (PFNa,p,m) to PFL3 pre-motor output neurons.

B) Indirect pathway from wind-sensitive PFNs to PFL3: left and right PFNs synapse onto hΔC neurons, which project halfway across the FB to FC neurons, which project to PFL3 neurons.

C) Mapping from wind direction input to turning motor output derived from behavioral data. Plot shows mean angular velocity as a function of initial egocentric wind direction, computed from behavioral responses to odor shown in Fig. 1C. Mapping shown here is taken over 1 second following odor offset, in the presence of wind only. Negative wind directions (wind from left) promote positive angular velocities (right turns), leading to stable downwind orientation. Cartoons depict fly turning at -90°, 0°, and 90° wind directions, as indicated by colored arrows to generate stable orientation.

D) Same as (C) for 1 second following odor onset. Here, negative wind directions (wind from left) promote negative angular velocities (left turns), leading to stable upwind orientation.

E) Predicted heading signals in wind-sensitive PFNs. Left and right hemisphere PFNs each receive a heading bump through the protocerebral bridge that is shifted 45° contralateral from the heading signal found in compass neurons (Hulse et al. 2021).

F) Predicted wind tuning in wind-sensitive PFNs. These PFNs show sinusoidal tuning to wind direction that is maximal at 45° ipsilateral (Currier et al. 2020). In the model, the amplitude of the activity bump on each side of the protocerebral bridge is modulated by wind direction so that its amplitude is maximal at 45° ipsilateral. Panel shows activity bump amplitudes of left and right PFNs in the protocerebral bridge (left) and vector representations (right) for four different wind directions.

G) Vector representation (left) and FB activity profiles (right) of PFN and hΔC activity. Right (blue) and left (orange) PFNs represent vectors whose angles are 45° contralateral to the fly midline, and whose amplitudes depend on wind direction. The net PFN signal in the FB (pink) represents the sum of these two vectors. Leftward wind (-90°) generates a net PFN signal shifted towards left PFN heading bump. hΔC projects half-way across the FB, resulting in 180° rotation of the net PFN vector (red). Leftward wind (-90°) generates an hΔC signal closer to the right PFN heading bump.

H) Predicted heading signals in PFL3 output neurons. Left and right hemisphere PFL3 neurons each receive a heading bump through the protocerebral bridge that is shifted 90° ipsilateral from the heading signal found in compass neurons (Hulse et al. 2021). Panel show activity profiles (top) and vector representations (bottom).

I) Turn computation in the direct pathway. Leftward wind generates a net PFN signal that is shifted towards the right PFL3 heading bump, leading to right turns (we assume here that PFL3 projects contralaterally but is inhibitory, leading to ipsilateral turns).

J) Turn computation in the indirect pathway. Leftward wind generates a net PFN signal that is shifted towards the left PFL3 heading bump, leading to left turns.

K) Predicted mapping from wind direction input to turning motor output in the direct pathway. Across all wind directions, the direct pathway generates stable downwind orientations.

L) Predicted mapping from wind direction input to turning motor output in the indirect pathway. Across all wind directions, the indirect pathway generates stable upwind orientations.

Supplementary Figure 6

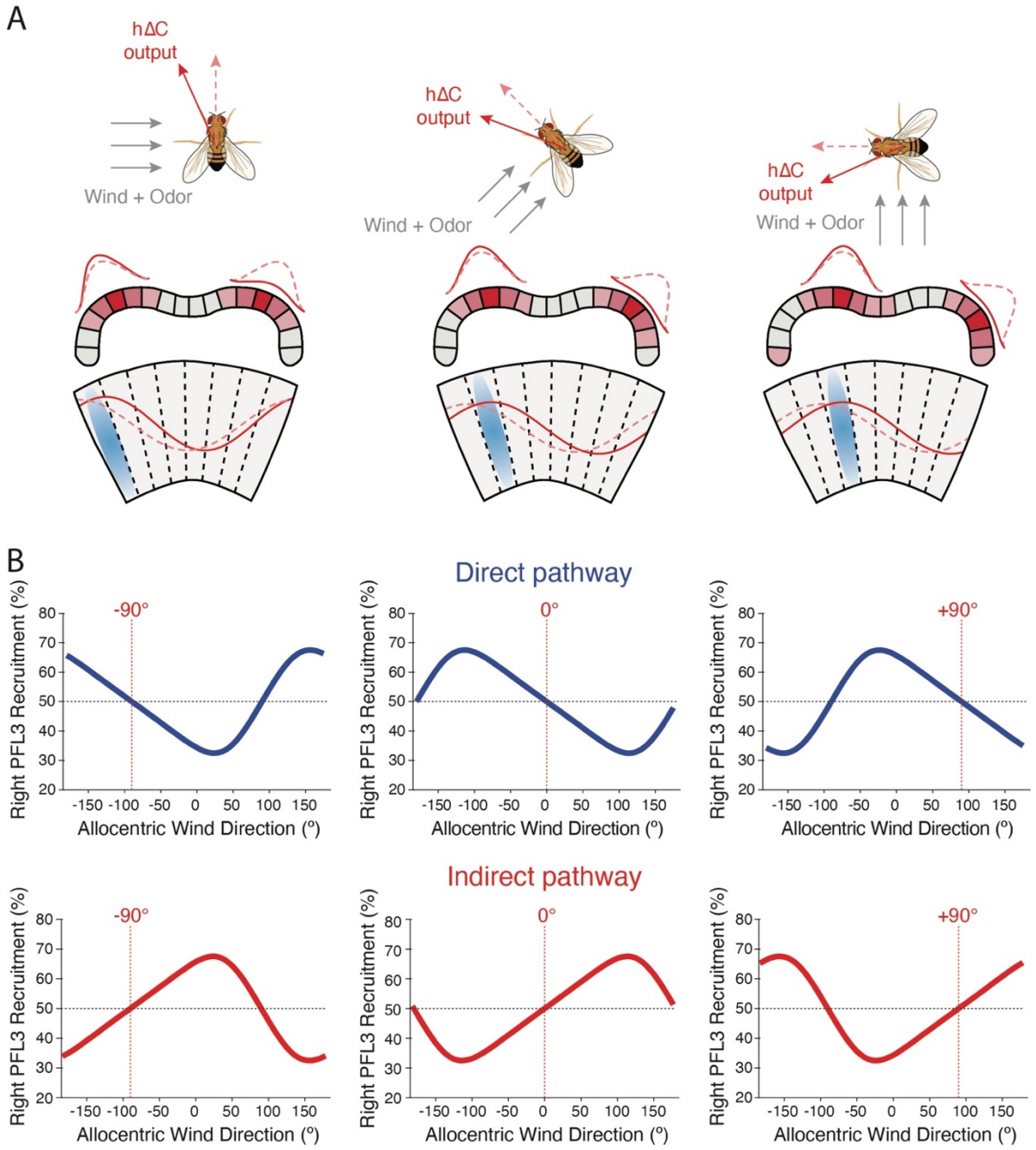

Fig. S6: Role of the heading compass in FB model of wind orientation.
A) Predicted hΔC activity bump depends on both fly heading and egocentric wind direction. We consider three different scenarios with equivalent egocentric wind direction (-90°) but different heading directions (left, 0°; middle, -45°; right, -90°). For comparison, the hΔC vector and sinusoid for frontal wind are also displayed (dashed lines). As the fly's heading rotates, the hΔC activity bump shifts linearly across the FB (blue: peak of activity bump). As the allocentric wind direction changes from frontal wind to leftward wind, the hΔC activity bump shifts by

approximately one FB column, regardless of the heading direction. Thus, heading determines the central location of the hΔC activity bump, while egocentric wind direction nudges the bump to the left or right of this central location.

B) Direct and indirect pathways generate egocentric wind orientation, regardless of absolute heading direction. As the absolute heading direction (red dashed line) is rotated from -90° (left) to 0° (middle) to +90° (right), the direct pathway shifts to generate stable downwind orientations at 90°, 180°, and -90° wind, respectively, while the indirect pathway shifts to generate stable upwind orientations at -90°, 0°, and 90° wind, respectively.

Supplementary Figure 7

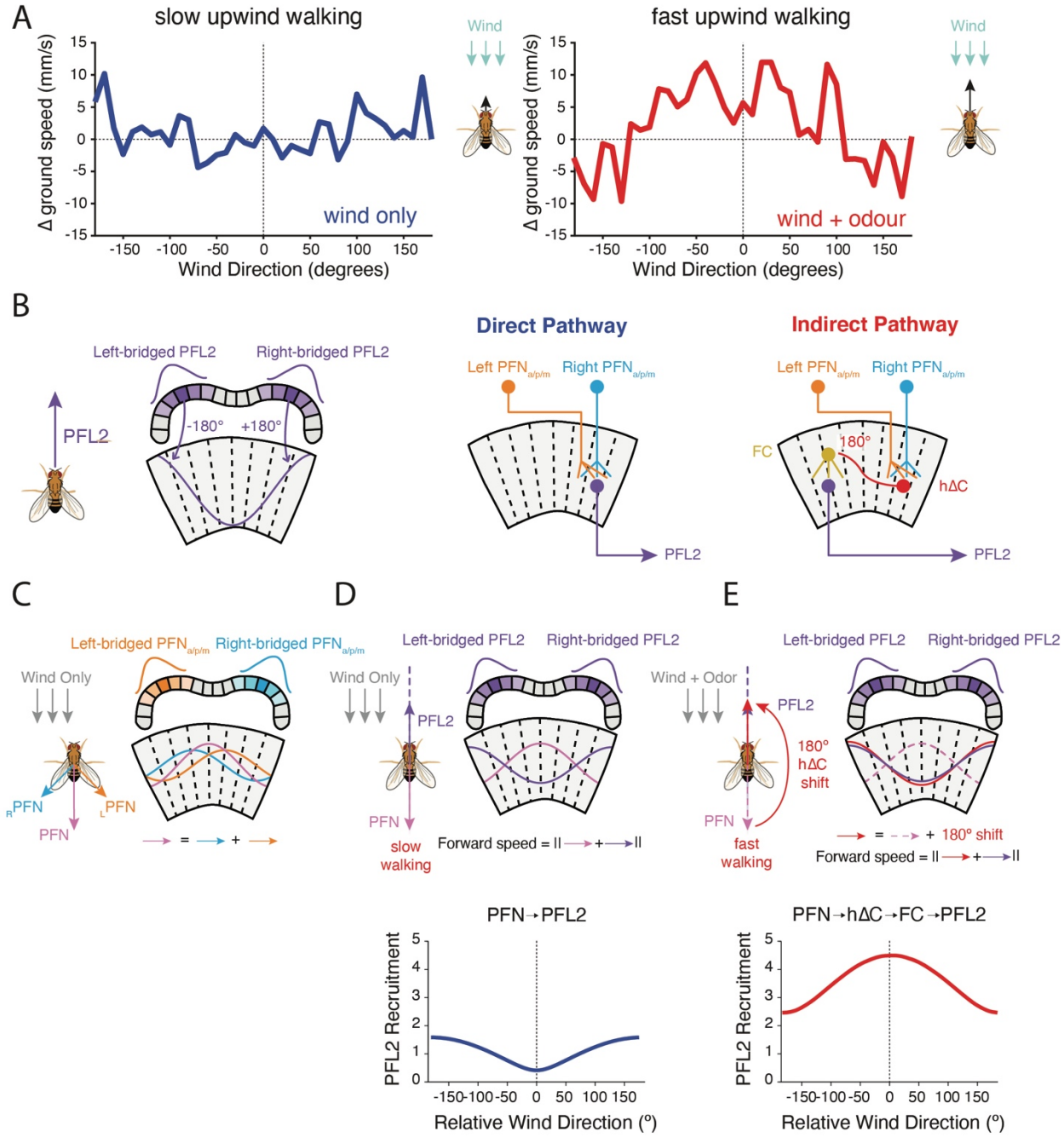

Fig. S7: A model for olfactory gating of wind-evoked forward velocity.

A) Mappings between egocentric wind direction and mean change in forward velocity, computed from odor response data shown in Fig. 1C. Positive wind directions indicate wind to the fly's right and positive ground speed indicates forward walking. Left: 0-1s after odor offset. Right: 0-1 s after odor onset. Cartoons depict fly ground speed at 0° wind direction.

B) Left: Predicted heading signals in PFL2 neurons. Left and right hemisphere PFL2 neurons each receive a heading bump through the proto-cerebral bridge that is shifted 180° ipsilateral

from the heading signal found in compass neurons (Hulse et al., 2021). Heading signals in PFL2 neurons are shown here both as vectors and sinusoids. Middle: In the direct pathway, left and right PFNs directly synapse with PFL2 neurons. Right: In the indirect pathway, left and right PFNs synapse onto hΔC neurons, which project 180° across the FB to FC neurons, which finally project to PFL2 neurons.

C) Frontal wind (0°) generates a signal in wind-sensitive PFNs centered between the left and right PFN heading bumps.

D) In the direct pathway, frontal wind generates a PFN bump that is completely out-of-phase with the PFL2 heading bump, leading to no forward walking (top). Across all wind directions, the direct pathway generates downwind walking (bottom).

E) In the indirect pathway, frontal wind generates a PFN bump that is shifted 180° by hΔC, making it completely in-phase with the PFL2 heading bump and leads to forward walking (top). Across all wind directions, the direct pathway generates upwind walking (bottom).

Figure 7

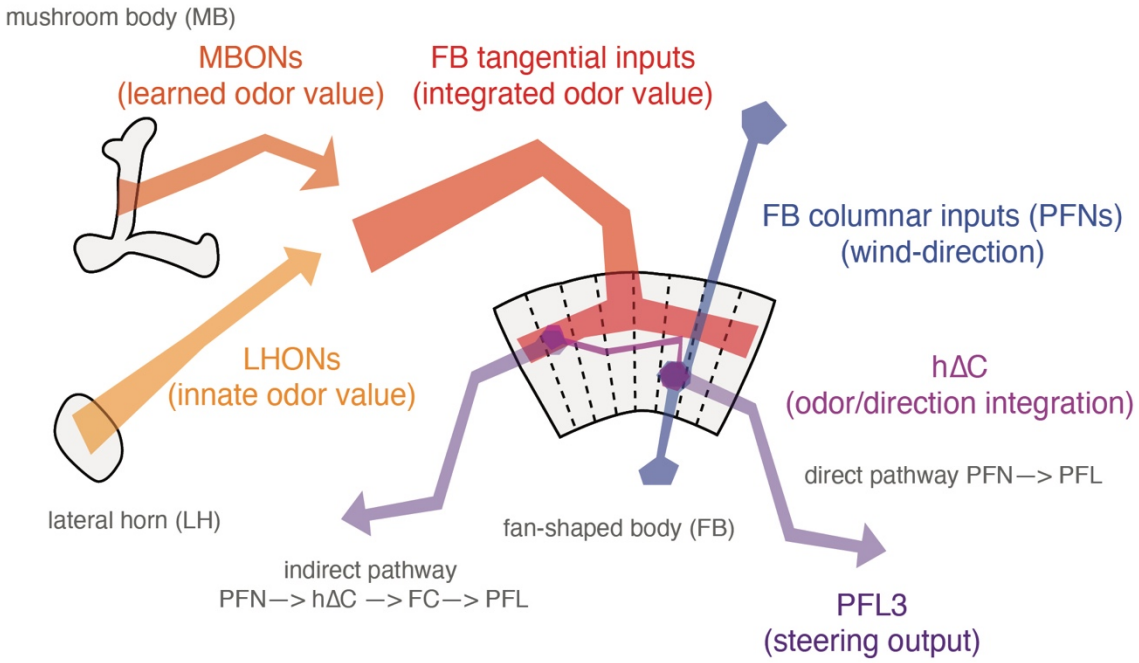

Fig. 7: Conceptual model of sensory integration for olfactory navigation in the *Drosophila* central brain

Conceptual model of central olfactory navigation circuitry as suggested by this and previous studies. MBONs and LHONs promote wind navigation and carry learned and innate odor information respectively, but do not encode wind direction. They thus represent a non-directional value signal that is combined with wind directional information downstream to generate navigational trajectories. FB tangential inputs are anatomically poised to integrate learned and innate information and we show here that they likewise encode a non-directional odor signal. In contrast, FB columnar inputs (PFNs) encode wind direction independent of odor presence. hΔC neurons receive input both from directionally-tuned PFNs and odor-tuned FB tangential inputs, and encode a multi-plexed odor-gated wind direction signal. Our data thus argue that the FB receives directional and non-directional input through its columnar and tangential input pathways respectively. PFL3 neurons are hypothesized to drive steering and receive input both from PFNs (direct pathway, promoting downwind orientation) and from hΔC neurons (indirect pathway, promoting upwind orientation). Odor input through FB tangential inputs alters the strength of competing pathways connecting PFNs to PFLs to drive context-appropriate changes in wind orientation behavior. Taken together, our data support a model in which FB tangential inputs allow for the selection of different navigational trajectories by gating information flow from direction-tuned FB columnar inputs (PFNs) onto FB output neurons (PFLs).